SCALE DEPENDENCE OF FRACTURE DENSITY AND FABRIC IN THE DAMAGE ZONE OF A LARGE DISPLACEMENT CONTINENTAL TRANSFORM FAULT

A Thesis

by

MUHAMMED FATIH AYYILDIZ

Submitted to the Office of Graduate Studies of
Texas A&M University
in partial fulfillment of the requirements for the degree of

MASTER OF SCIENCE

Approved by:

Chair of Committee,   Judith S. Chester
Committee Members,   Frederick M. Chester
                       Ibrahim Karaman
Head of Department,   Rick Giardino

December 2012

Major Subject: Geology

ABSTRACT

Characterization of fractures in an arkosic sandstone from the western damage zone of the San Andreas Fault (SAF) at San Andreas Fault Observatory at Depth (SAFOD) was used to better understand the origin of damage and to determine the scale dependence of fracture fabric and fracture density. Samples for this study were acquired from core taken at approximately 2.6 km depth during Phase 1 drilling at SAFOD. Petrographic sections of samples were studied using an optical petrographic microscope equipped with a universal stage and digital imaging system, and a scanning electron microscope with cathodoluminescence (SEM-CL) imaging capability. Use of combined optical imaging and SEM-CL imaging was found to more successfully acquire true fracture density at the grain scale. Linear fracture density and fracture orientation were determined for transgranular fractures at the whole thin section scale, and intragranular fractures at the grain scale. The microscopic scale measurements were compared to measurements of mesoscopic scale fractures in the same core, as well as to published data from an ancient, exhumed trace of the SAF in southern California. Fracturing in the damage zone of the SAF fault follows simple scaling laws from the grain scale to the km scale. Fracture density distributions in the core from SAFOD are similar to distributions in damaged arkosic sandstone of the SAF along other traces. Transgranular fractures, which are dominantly shear fractures, indicate preferred orientation approximately parallel to the dominant sets of the mesoscale faults. Although additional work is necessary to confirm general applicability, the results of this work demonstrate that fracture density and orientation distribution over a broad range of scales can be

determined from measurements at the mesoscopic scale using empirical scaling

relations.

DEDICATION

To my family

ACKNOWLEDGEMENTS

TABLE OF CONTENTS

LIST OF FIGURES

LIST OF TABLES

1. INTRODUCTION

Faults in the crust are characterized by relatively thin zones of localized shear, referred to as the fault core, which are bounded by much thicker zones of variably deformed rock called damage zones (Figure 1) [e.g., *Chester et al.*, 2005]. Characterizing the damage zones of faults is important to understanding earthquake energetics, fluid flow in the crust, and the mechanics of deformation of the crust. Much of what we know about damage states of faults in the subsurface is based on geologic study of inactive, exhumed faults. An example is provided by a series of structural and petrologic studies of the Punchbowl Fault, an ancient exhumed fault of the San Andreas system in southern California [*Chester and Logan*, 1986; *Chester et al.*, 1993; *Chester and Chester*, 1998; *Chester et al.,* 2004; *Schulz and Evans*, 1998, 2000; *Wilson et al.*, 2003]. The Punchbowl Fault studies, and similar work on other inactive exhumed faults [e.g., *Mitchell and Faulkner*, 2009; *Faulkner et al.*, 2011; *Holdsworth et al.*, 2011], often are given as type examples for the structure of active faults at depth [e.g., *Imber et al.*, 2008]. This view, however, comes with some uncertainty because inactive, exhumed faults often display chemical alteration and deformation overprinting associated with uplift and exhumation [e.g., *Solum et al.*, 2006].

In recent years, the opportunity to study the in situ structure and chemistry of active faults at depth has been provided through deep scientific drilling and sampling [*Ohtani et al.*, 2001; *Cornet et al.*, 2004; *Tobin and Kinoshita*, 2006; *Zoback et al.*, 2006; *Ma et al.*, 2006]. The San Andreas Fault Observatory at Depth (SAFOD) is a particularly noteworthy effort to drill into an active fault zone that successfully

transected and sampled the San Andreas Fault (SAF) zone at approximately 2.6 km

depth [*Scholz*, 2000; *Hickman et al.,* 2004; *Boness and Zoback*, 2006; *Solum et al*., 2006;

Bradbury et al., 2007; *Draper et al*., 2009; *Zoback et al*., 2010; *Holdsworth et al.*, 2011].

Damaged rocks collected from the western damage zone at SAFOD include densely

fractured, arkosic pebbly sandstone. This sandstone is similar to the Punchbowl

Formation arkosic sandstone found along the Punchbowl Fault in Devil's Punchbowl

County Park, California [i.e., *Chester et al.,* 2004, *Almeida*, 2007; *Dor et al*., 2009].

Similarities include composition, depth of faulting, fracture state, and secondary

alteration and cementation products (*Table 1*).

Studies of exhumed faults have demonstrated that the damage zones of faults

evolve significantly in the early stages of the fault growth, but evolve much more slowly

at large displacement [e.g., *Chester and Chester,* 1998]. Quantification of damage

intensity with distance from the master fault surface shows that at the early stages, the

thickness of the damage zone and magnitude of damage increase with displacement.

Damage zone characteristics in faults with displacement greater than a km, however,

evolve very slowly, such that the total thickness and damage intensity of many large

displacement faults are approximately the same [e.g., *Savage and Brodsky,* 2011;

Faulkner et al., 2010; *Mitchell and Faulkner,* 2012]. Studies of both microfracture and

mesoscopic scale fracture density at the large-displacement Punchbowl Fault were used

by *Chester et al.* [2005] to quantify the total surface area of fractures within the damage

zone as a means to constrain the energy budget of faulting. For their analysis they used

assumptions of power-law scaling of fracture density with fracture size (length)

2

constrained by the measurement of fracture density at the two scales. These assumptions, however, have not been tested rigorously or further constrained by additional measurements. The apparent similarity of deformation in the arkosic pebbly sandstones at SAFOD and the Punchbowl Formation at Devil's Canyon provide an opportunity to further investigate the scaling relationships for both fracture density and fracture fabric as a function of scale within the damage zones of two large displacement faults (Figure 2).

I propose to characterize the damage in the arkosic sandstone of the western damage zone at SAFOD to test the universality of the relations inferred from studies of the Punchbowl Fault in the Devil's Punchbowl Country Park, Los Angeles, and to use the data to better understand the origin of damage along the SAF at SAFOD, Specifically, I will characterize the orientation and density distribution of fractures at the whole thin section scale and at the intragranular scale of observation, using both optical and electron microscopy (i.e. petrographic, cathodoluminescence, and back-scatter electron imaging) imaging. In addition, I will use scanning electron-cathodoluminescence imaging (SEM-CL) to better determine true density of microfractures in the rock. The proposed work of *R. Almeida* [2007]; specifically, the proposed measurements will be compared to and analyzed in terms of published and unpublished data for the same rocks provided by *R. Almeida* at the mesoscale, and to similar data sets for other major continental fault zone, including the Punchbowl Fault, an ancient, exhumed trace of the SAF in southern California.

2. BACKGROUND

2.1 The San Andreas Fault

The SAF is an active, right-lateral, continental transform fault that juxtaposes the North American and Pacific Plates [*Catchings et al.,* 2002]. The SAF is about 1300 km long and consists of multiple principal fault strands with three major fault segments. A central segment lies between Cholame and San Juan Batista, California, a northern segment extends offshore at Cape Mendocino, California, and a southern segment extends to the Bombay Beach Area in the southern California (Figure 3). The width of damaged rock surrounding the SAF zone ranges from a few hundred meters to several kilometers [e.g., *Holdsworth et al.,* 2011]. Both the southern and the northern segments of the SAF tend to slip in large magnitude earthquakes, whereas the middle segment creeps at about 25 mm/yr and displays continuous microseismicity [*Savage and Burford,* 1971; *Titus et al.,* 2006].

2.2 The San Andreas Fault Observatory at Depth

The National Science Foundation Earth Scope program established the SAFOD. At the surface, this natural research observatory is located 1.8 km west of the SAF near Parkfield, California at the transition from the creeping segment of the fault to the north and the locked segment to the south. The scientific borehole crosses the SAF at 2.5 – 3 km depth (Figures 4). The SAFOD project provides subsurface data including geophysical logs, spot core samples from inside and outside the fault zone, and continuous seismological and geophysical monitoring data [*Zoback et al.,* 2010]. The purpose of the SAFOD project is to better understand earthquake processes along a

4

major plate boundary fault zone at seismogenic depths. The specific objectives of this

drilling and observatory are to provide a detailed description of the composition and

structure of the fault, determine the dominant deformation mechanisms operating within

the fault zone, estimate the in situ pore pressure and principal stress state of the fault,

and to investigate the role of fluid-rock reactions during fault creep in the region

intersected by the borehole [e.g., *Zoback et al.,* 2007]

Drilling at SAFOD initiated with a 2.2 km-deep, vertical pilot hole that was

drilled 1.8 km west of the surface trace of the SAF [*Zoback et al.,* 2007]. The main

borehole, located just east of the pilot hole, was drilled in three phases in 2004, 2005,

and 2007, and houses the observatory (Figure 4). This hole is vertical to 1.5 km depth,

and inclined about 60˚ from the vertical to the northeast, reaching a total vertical depth

of 3.2 km on the east side of the SAF. The SAFOD borehole penetrates the Salinian

granites at 1460 m and arkosic sandstones/conglomerates at 2507 m. These rocks were

sampled by unoriented spot coring during Phase 1 drilling. This study focuses on the

11.6 m of fractured and faulted arkosic sandstone retrieved during Phase 1 spot coring

(Figure 4). A large subsidiary fault, located at 3067 m measured depth along the

borehole (MD), was captured at the base of the Phase 1 arkosic sandstone. According to

zircon fission-track analysis, the age of this arkosic section ranges from late Cretaceous

to early Paleocene (70 – 62 Ma) [*Draper et al.*, 2009].

Another section of arkosic sandstone was cored during Phase 3 drilling. This spot

core was taken at a total depth of 3.2 km. The presence of an additional large subsidiary

fault between the Phase 1 and Phase 3 arkosic sandstone units has been inferred on the

basis of a significant change in bedding, between 3126 – 3134 m MD. This change in bedding is evident in the image logs taken during Phase 2 [*J.S. Chester, personal communication*, 2011]. Two narrow zones of active creep also were cored during Phase 3, the Southwest Deforming Zone (SDZ) at 3192 m MD, and the Central Deforming Zone (CDZ) at 3302 m MD [*Zoback et al.,* 2011]. The horizontal distance between the SDZ and the base of the Phase 1 arkosic sandstone investigated in this study is about 90 m.

Almeida [2007] carried out a comprehensive mesoscale structural characterization of the granodiorite and sedimentary rock spot cores taken during Phase 1. He specifically described the orientation and densities of mescoscale fractures cutting the core [*Almeida*, 2007], and the microfracture orientations within key samples taken from the core [*J. Chester, personal communication*, 2011]. Later, Heron also performed a more detailed analysis of the mesoscale fracture density analysis of the same core section [*J. Chester, personal communication*, 2011]. The results *Almeida* [2007] and *Heron* [2011] will be used and built upon in this study.

2.3 Structure of the San Andreas Fault at 0 – 3 km Depth

2.3.1 Macroscopic Structure

At the macroscopic scale, a brittle fault may be defined as a tabular zone of brittle deformation. The thickness of this zone is much less than length and width, and the shear displacement parallel to the zone is significantly greater than the thickness of the zone. Large displacement strands of the SAF system have achieved tens to hundreds of km of shear displacement. These large displacement fault zones may be described in

terms of three basic structural units: the undeformed rock, the damage zone, and the fault core (Figure 1) [e.g., *Chester et al.,* 1993; *Caine et al.,* 1996]. The fault core is characterized as a relatively narrow zone containing products of high shear strain, such as ultacataclasites, cataclasites, breccias, and gouge layers [e.g., *Wallace and Morris,* 1986; *Chester and Chester,* 1998], and generally accommodates a large fraction of the total shear displacement of the fault. The fault core often contains mesoscopic scale slip surfaces and other evidence of shear localization [*Chester and Chester,* 1998; *Chester et al.,* 2005]. The damage zone generally is much thicker than the fault core. The damage zone represents a transition zone between the fault core and undeformed host rocks (Figure 1). In general, deformation intensity in the damage zone decreases with distance from the fault core and forms a gradational boundary with the undeformed host rock [e.g., *Chester and Chester,* 1998; *Savage and Brodsky,* 2011].

In detail, the geometric characteristics of fault zones can be variable [e.g., *Wallace and Morris,* 1986; *Faulkner et al.,* 2011]. A common geometrical model for the fault zone is a single fault core approximately centered in a damage zone [e.g., *Chester et al.,* 1993], however, fault zones may contain several distinct fault cores that may form a braided network within a broad, heterogeneous damaged zone [e.g., *Faulkner et al.,* 2011]. The active SAF trace at Littlerock and the exhumed Punchbowl Fault in Los Angeles County are best described as single or paired fault core systems, whereas it appears that the active SAF at depth at SAFOD consists of several fault cores [e.g., *Zoback et al.,* 2011].

2.3.2 Mesoscopic Structure

Damage zones are characterized by a prevalence of deformation structures including folded strata, fractures (e.g., subsidiary faults and joints), veins, solution seams, comminuted grains, microfractures, and localized alteration and mineralized zones [e.g., *Chester et al.,* 2004]. For brittle faults in sedimentary rocks, such as the SAF at SAFOD and at Littlerock, and the Punchbowl Fault, the dominant structural features often are fractures, and very close to the fault core, cataclastic zones. To a variable extent, the density and orientation distributions of mesoscale fractures at each of these locations have been characterized as a function of scale and position (*Table 2*).

The intensity of mesoscale fracturing can be quantified by a linear fracture density, which is determined by counting the intercepts of fractures with a count line and is reported as the number of intercepts per unit length [e.g., *Chester et al.,* 2005]. For many fault zones studied to date, the fracture density (or log of fracture density) in the damage zone decreases linearly with the logarithm of distance from the fault core [e.g., *Savage and Brodsky,* 2011]. At the Punchbowl Fault, the mesoscale fracture density varies from more than 100/m near the fault core, to around 15/m at 100 m from the fault core, which is the location of the boundary with the undeformed host rock [*Wilson et al.,* 2003]. The data also display clear local variations near large subsidiary faults. *Chester et al.* [2005] use these observations to support the interpretation that the fracture density in damage zones scales with fracture length, according to a power law. The mesoscale fracture density in the arkosic sandstone cored during Phase 1 drilling at SAFOD, was estimated by *R. Almeida* and *B. Heron* [*J.Chester, personal communication*, 2011].

8

Although these estimates only define the fracture density at a specific distance from the SDZ and CDZ, and not the linear fracture density as a function of distance from the two actively creeping fault traces, the estimates are critical to understanding the origin and character of damage zones along plate boundary faults in the continental crust. A mesoscale fracture density has not yet been reported for the Juniper Hills Formation at Littlerock, California [*Dor et al.,* 2009].

The mesoscale subsidiary fault fabric has been characterized for the damage zone of the Punchbowl Fault [*Chester and Logan,* 1986; *Wilson et al.,* 2003], and for the Phase 1 arkosic sandstone core from SAFOD [*Almeida,* 2007]. In both cases, the fabrics are characterized as quasi-conjugate sets of strike-slip faults that are defined by a bisector that is oriented at a high angle to the master fault, indicating that the shortening direction also is oriented at a high angle to the master fault plane. The quasi-conjugate set at SAFOD, however, is defined by a larger dihedral angle, when compared to that at the Punchbowl Fault, suggesting that the mesoscale faulting in the SAFOD damage zone occurred at somewhat higher effective mean stress. Mesoscale fault fabric data have not been reported for the San Andreas Fault at Littlerock [*Dor et al.,* 2009].

2.3.3 Microscopic Structure

Some intensity and orientation data for microfractures at the grain scale, i.e., intragranular fractures, have been reported for all three locations discussed above; but, to date there has been little analysis of data defining the intensity and orientation of transgranular cracks (those that cut two or more grains at the scale of an entire petrographic thin section) in the literature.

The intragranular fracture density has been characterized for the San Andreas Fault at Littlerock and for the Punchbowl Fault at Devil's Punchbowl County Park [*Dor et al.,* 2009; *Wilson et al,.* 2003]. Although the techniques used to quantify the intragranular fracture density at these two sites are somewhat different, the fracture density at both locations follows a linear dependence on the log of distance from the fault core. This relationship is similar in functional form to that seen for the mesoscale fracture density at the Punchbowl Fault [*Wilson et al.,* 2003]. The linear density of intragranular microfractures at the Punchbowl Fault varies between more than 70/mm, near the fault core, to a background level of about 20/mm, at a distance of 100 m or greater from the fault core. This grain-scale density is consistent with the power-law scaling relation used by *Chester et al.* [2005] to characterize the size-frequency relationships for mesoscale subsidiary faults. That the size-frequency relations for these two features are similar is somewhat perplexing, because the intragranular microfractures are Mode 1 (i.e., opening mode) cracks whereas the subsidiary faults are shear cracks. The density of two distinctly different types of fractures should not necessarily scale by the same relationship. Size-frequency relations at the transgranular fracture scale (i.e., at the scale of a petrographic microscope thin section) need to be quantified for several fault zones to better constrain these relationships.

At the Punchbowl Fault, intragranular microfractures display diffuse but preferred orientations that are compatible with the mesoscale subsidiary fault fabrics. Specifically, intragranular microfractures tend to have preferred orientations at high angles to the master fault plane, and that bisect the conjugate subsidiary fault set, as

10

would be expected [*Wilson et al.,* 2003]. Intragranular microfracture orientations measured in the Juniper Hills Formation along the San Andreas Fault at Littlerock, California, also show a preferred orientation that is at a high angle to the master fault [*Dor et al.,* 2009]. This is the case even though the Littlerock measurements were made on petrographic thin sections from only one orientation (parallel to the horizontal plane), rather than on three mutually perpendicular thin sections. Preliminary microfracture orientation data from the arkosic sandstone collected during Phase 1 drilling at SAFOD, however, appear to define a much more diffuse pattern [*unpublished data of Almeida,* 2007; *J.Chester, personal communication,* 2011], even though the mesoscale subsidiary fault fabric in the core is very distinct [*Almeida,* 2007].

Petrographic studies show that there is relatively little secondary mineralization in the Juniper Hills Formation at Littlerock, California, consistent with a very shallow depth of burial and deformation [*Dor et al.,* 2009]. In contrast, the arkosic sandstones at SAFOD and those adjacent to the Punchbowl Fault show extensive, syntectonic cementation, primarily by laumontite [*Wilson et al.,* 2003; *Heron,* 2011]. Based on cross-cutting relations, *Wilson et al.* [2003] suggest that much of the microfracturing in the Punchbowl Formation occurred after secondary cementation by laumontite.

3. METHODS

3.1 Sample Description

The 11.6 m of fractured and faulted arkosic sandstone retrieved during Phase 1 coring was taken between 3055 and 3067 m MD (Figure 4). The upper portion of this sequence (between 3055 and 3062 m MD) consists of pebble conglomerate to coarse-grained sandstone that has clasts of granite and volcanic rocks within massive, well-cemented beds [*Almeida*, 2007]. My samples were taken from this upper unit. Five samples were chosen from the less deformed portion of the core and three samples were taken across mesoscale subsidiary faults described in detail by *Heron* [2011] (Figure 5). Using these samples, I have characterized the fracture intensity, fracture orientations, and cross-cutting structural relations at two scales of observation, the whole thin-section scale and the intragranular scale. To do this, three mutually perpendicular petrographic thin sections were made from the less deformed samples (*Table 3*). These sections are defined by outward normal to each thin section plane and are referenced to the borehole orientation and Geographic North, according to the convention described in *Almeida* [2007]. One petrographic thin section was prepared from each of the three mesoscale fault samples. The orientation of each of these latter sections is perpendicular to the plane of the mesoscale fault and parallel to the estimated slip-direction of the fault. All samples are listed on *Table 3*.

The trangranular and intragranular fracture intensity data were collected on a petrographic microscope equipped with a mechanical stage, and the transgranular fracture orientation data were collected using a four-axis universal stage mounted on a

petrographic microscope equipped with a mechanical stage, and the transgranular

fracture orientation data were collected using a four-axis universal stage mounted on a

petrographic microscope. In addition, intragranular fracture intensity data also were

acquired from select grains within the small fault samples using a FEI Quanta 600 FE-

SEM equipped with a back-scattered electron detector and a Gatan panchromatic

cathodoluminesce detector that has a Zyvex S100 nanomanipulator and RGB filters.

For this study, transgranlar fractures are defined as those features that cut more than two

grains. Transgranular fractures types distinguished are fractures that (1) display no shear

within the plane of the thin section and that are either open or sealed (i.e., veins) (2)

shear fractures with and without gouge. Intragranular fractures are defined as those that

are contained within one grain. These latter fractures are classified open, healed, or

sealed, after *Friedman* [1969] and *Wilson et al.* [2003].

Plane- and cross-polarized light digital image scans, at a scale of 157.5 pixels per

mm, were taken of each thin section and used as location map for the fracture intensity

and orientation measurement (Figure 6).

3.2 Petrologic Descriptions

To define the mineralogic variation in this portion of the core, five representative

thin sections (*Table 3)* were stained to distinguish plagioclase feldspar, potassium

feldspar, and quartz. To stain potassium feldspar yellow [e.g., *Gabriel and Cox,* 1929],

the sections were dipped in barium chloride solution and treated with cobaltinitrite [e.g.,

Gabriel and Cox, 1929]. To stain plagioclase feldspar red the sections were treated with

potassium rhdizonate [*Bailey and Stevens,* 1960]. For each section, the volume percent

of each mineral phase was determined by standard point count methods [e.g., *Dickinson,* 1970; *Draper et al.,* 2009] on a petrographic microscope equipped with a mechanical stage. Mineral determinations were made at every intersection on a 0.08 mm square grid, producing about 1050 point counts per thin section.

3.3 Linear Fracture Density Estimates

3.3.1 Transgranular Fracture Intensity

At the whole thin-section scale, I made two linear fracture density estimates to explore scale dependence using an intercept technique similar to that described by *Anders and Wiltschko* [1993], *Neal* [2002], and *Takagi et al.* [2012]. For the first estimate, the number of transgranular fractures that intercepted an 8 mm square grid was counted. The second estimate used a 3 mm square grid. For each grid direction, the number of fracture intercepts with the grid lines were divided by the total length of the grid lines to give the linear transgranular fracture density (LTGFD) as a function of direction. To determine the LTGFD for the sample, the average of the two directional values was recorded. In addition to the number of fracture intercepts, the type of each fracture (i.e., open, sealed, cataclastic zone, gouge zone), composition of fracture fill (e.g., calcite), and length of each fracture were noted.

3.3.2 Intragranular Fracture Intensity

The number of intragranular microfractures was counted using a traverse method modified from *Anders and Wiltschko* [1993] and *Neal* [2002]. The fracture counts were made in about fifty-five to sixty quartz grains, larger than 0.58 mm in diameter that fell on or near the intersection points of a 2 mm square grid placed on the whole thin section.

Combining the data for the three mutually perpendicular thin sections made from each sample provided a total of 165 to 180 analyzed grains per sample. Feldspar grains were used in quartz-poor samples, when necessary. Within each grain, the number of fractures intersecting a count line was recorded. The orientation of the count line was defined by a list of random numbers from 0 to 360 used in sequence. The count line was place along the longest dimension of the grain in the orientation specified by the number sequence. The orientation of the line, length of the line, number of fracture intercepts, and fracture type (i.e., open, healed, sealed) were recorded.

3.3.3 Intragranular Fracture Intensity Using SEM-CL

Sometimes intragranular fractures, especially sealed and healed fractures, and cross-cutting relations, are not visible when samples are viewed with a petrographic microscope, but may be visible using catholuminescence (CL) imaging on a scanning electron microscope (SEM) [e.g., *Milliken and Laubach,* 2000]. This imaging technique can detect variations in luminescence intensity within different parts of grains that are related to subtle variations in structure and chemistry. In sandstone, SEM-CL imaging is particularly useful to detect different generations of cement, alteration products, and fracture events, particularly in quartz grains [*Laubach,* 1997]. I used SEM-CL imaging specifically to quantify the total number of observable fractures intersection a 100 micron square grid in select quartz grains, and compared these data to the same type of data acquired at the same magnification (e.g., Ocular magnification of P1 10X/25 and Objective magnification of 20X/0.5pol) using a Zeiss Axioplan 2 Petrographic Microscope. These data are used to determine if the optical grid intersection method

underestimates the fracture intensity for these samples. For this study the acquisition time per CL image was 13 minutes, so to capture the RGB filter sequence required about 1 hour.

3.4 Transgranular Fracture Orientations

The orientations of the transgranular fractures were measured from three mutually perpendicular petrographic thin sections, taken from five relatively undeformed samples (P1B11-1, P1B13-1, P1B14-1, P1B16-2, and P1B17-4; *Table 3*) using a universal stage mounted on a petrographic microscope following the methods described by *Friedman* [1969]. For non-planar transgranular fractures, I recorded the average orientation for each major line segment of a fracture. Segment orientations and fracture type (open, sealed, and shear fractures) were recorded in an excel spreadsheet, and mapped and numbered on the image scans using Photoshop. The orientations of the transgranular fractures were plotted in lower hemisphere, equal-area stereographic projections OSXStereonet v.1.7 by *N. Cardozo* and *R. Allmendinger* [2011].

3.5 Cross-cutting Relations between Structural Elements and Alteration Products

To understand the origin and evolution of the western damage zone of the SAF at SAFOD, cross-cutting relations for different fracture sets and the timing of cementation events relative to fracturing were analyzed using a petrographic microscope, SEM-CL imaging, and back-scatter electron (BSE) imaging.

4. RESULTS

4.1 Petrology

Quantification of mineral composition helps to understand deformation history and related diagenetic events. Therefore, standard point count method [e.g. *Dickinson,* 1970; *Draper et al.*, 2009] was applied to five representative thin sections from the arkosic sandstone interval of the SAF at SAFOD (*Table 3*). The point count results exhibit modal compositions ranging from 27% to 35% quartz, 17% to 45% feldspar, including variable amount of plagioclase, orthoclase, and oligoclase, and consisting of clay minerals, commonly laumontite and illite.

From the sample thin sections, it is observed that quartz grains are fractured, and most of them indicate patchy and undulatory extinction. Plagioclase feldspar grains, which have rich sodium, are generally fractured and also consist of mica inclusions. Orthoclase feldspar grains are relatively unaltered; however, some of them show fractures due to cleavage.

Two major cement types (1) calcite and (2) laumontite are determined in the sample thin sections. These cements are present to be either pore filling or sealing of some transgranular, intragranular, and grain boundary microfractures. Additionally, some samples indicate that calcite or laumontite cement in an intragranular microfracture connects to cement in adjacent pore space.

4.2 Microfracture Types

According to microscopic analysis, I observed mainly three types of microfractures: (1) transgranular fractures, (2) intragranular fractures, and (3) grain

17

boundary fractures from the thin sections under optical microscope.

The total number of transgranular fractures counted in the analysis from five samples (P1B11-1, P1B13-1, P1B14-1, P1B16-2, and P1B17-4) is 530. Each type of transgranular fractures, shear, sealed (vein), and open fractures, accounts for 54.7, 18.86 and 23.74%, respectively. Grain boundary fractures were not counted and measured; however, some grain boundary fractures, which cut a grain while following the boundary of another grain, were counted as transgranular fractures in this study.

Intragranular fractures are contained within one grain. Under the universal-stage microscope, three kinds of intragranular fractures were observed: (1) healed microfractures, which are healed by quartz and recognized by a planar array of fluid inclusions; (2) sealed microfractures, which are filled with laumontite, calcite, small particles, or iron hydroxides; and (3) open microfractures. The three types of intragranular fractures were counted from eight samples (P1B11-1, 12-1_3T, P1B13-1, P1B14-1, 15-1_1T, P1B16-2, 16-1_4T, and P1B17-4). Healed, sealed and open microfractures account for 83.5, 7.5 and 9% of the intragranular fractures, respectively.

4.3 Fracture Intensity

4.3.1 Transgranular Fracture Intensity

The linear transgranular fracture density determined from whole thin section mapping for each samples with their three perpendicular thin sections measured using grids with 8 mm line spacing are shown in detail in *Table 4* . The linear transgranular fracture density is ranging from 0.034#/mm to 0.196#/mm. The highest density was measured from P1B13-1 and the lowest from P1B11-1.

In addition to using grid with 8 mm line spacing (coarse spacing), grid with 3 mm line spacing (fine spacing) was used to measure the linear transgranular fracture density determined from whole thin section mapping for all samples (*Table 5*). The linear fracture density measured from 3 mm grid is ranging from 0.033#/mm to 0.184#mm. Like 8 mm grid results, 3 mm grid results indicate that the highest density was measured from P1B13-1 and the lowest density from P1B11-1. If the linear transgranular fracture density values from 8 mm and 3 mm grids are compared, density values from 8 mm grid are higher than 3 mm grid except for P1B16-2 (*Table 5*). Additionally, the average linear transgranular fracture density from two grids varies from 0.033#/mm to 0.190#/mm (*Table 5*)

Mesoscale faults that are near and/or cut the samples may influence the transgranular fracture density. The number of mesoscale faults that cut or are near each sample are listed in *Table 5*. It is seen that the linear transgranular fracture density increases with an increase in number of mesoscale faults. For instance, more mesoscale faults are counted near P1B13 than near P1B11, and the linear transgranular fracture density value of the P1B13 is greater than P1B11 (*Table 5*).

To reveal the variation of the linear transgranular fracture density with distance from the subsidiary fault, all measured linear transgranular fracture density values were plotted as a function of the distance to the large subsidiary fault, located at 3062.5 m MD (Figure 7). According to this graph, the linear transgranular fracture density increases linearly with the distance to the subsidiary fault. Although this graph shows a linear trend between fracture density and distance to the subsidiary fault, the data are scattered.

19

Therefore, it is concluded that there is no distinctive linear relations between transgranular fracture density and distance from the subsidiary fault.

4.3.2 Intragranular Microfracture Intensity

The linear intragranular fracture density determined from whole thin section traverse technique for all samples is shown in detail in *Table 6*. The linear intragranular fracture density ranges from 9.22#/mm to 13.97#/mm. The highest density was measured from P1B15-1_1T and the lowest one from P1B14-1.

Healed, sealed and open microfractures account for 83.5%, 7.5%, and 9% of intragranular microfractures, respectively (*Table 6*). The most common type of intragranular fracture are healed fractures. Therefore, the linear density of intragranular fracture should be mostly composed of intensity of healed fractures

To document variation of the linear intragranular fracture density with distance to the subsidiary fault, all measured linear intragranular fracture density values were plotted as a function of the distance from the large subsidiary fault, located at 3062.5 m MD (Figure 8). According to this graph, the intragranular linear fracture density does not show significant change. P1B12-2, P1B15-1, and P1B16-1 have relatively higher linear intragranular fracture densities (Figure 8). These samples also include small (1-2 mm thick), big (up to 10 mm thick), and intermediate (2-3 mm thick) subsidiary faults.

4.3.3 Intragranular Fracture Density Using SEM-CL

Five quartz grains from 12-2_3T and six quartz grains from 15-1_1T were chosen to investigate the intragranular fracture density determined using SEM-CL and optical imaging. Image of these quartz grains with diameter ranging from 0.2 mm to 0.98

mm were taken using both SEM-CL and the optical microscope to compare linear fracture density. All fractures in the quartz grains are not visible on both CL and optical image. When some fractures are able to seen on CL image, the same fractures may be invisible on optical image or vice versa. Differences in fracture characterization from the CL images and optical images of the same grain can be seen in representative images on Figure 9. For instance, more fractures can be identified in the CL image (Figure 9b). Additionally, some healed fractures, visible on CL image, are not visible or are difficult to recognize on optical images (Figure 9a). It is noted that different parts of the same grain shows luminescence variation. Therefore, the quality of CL images also plays a role in seeing the fractures.

To compare the two techniques, the total number of common fracture intercepts counted from composite fracture maps, created using both the SEM-CL and optical images, is subtracted from total number of fracture intercepts counted from CL image and optical image. These data are used to determine the true linear fracture density (Figure 9c, d, and e).

The total number of fracture intercepted counted from CL and optical images of six quartz grains and true linear fracture density of sample 12-2_3T are shown in *Table 7*. The total number of fracture intercepts on CL images of quartz grains is 252, whereas it is 219 for the optical images. The true linear fracture density for six quartz grains in sample P1B12-2_3T ranges from 29.6#/mm to 44.2#/mm, averaging 34.7#/mm (*Table 7*). The total number of fracture intercepts counted on the CL and optical images of five quartz grains and the true linear fracture density of sample 15-1_1T are shown in *Table*

7. The total number of fracture intercepts on CL images of quartz grains is 149, whereas it is 131 for the optical images. True linear fracture density for five quartz grains in sample P1B15-1_1T ranges from 28.2#/mm to 40.2#/mm with an average of 33.7#/mm (*Table 9*).

Using these data, a correction factor for the true linear fracture density is calculated using linear fracture density from the whole-thin section traverse technique and the true linear fracture density from the imaging technique (*Table 8 and 10*). The average calculated correction factor from six grains for sample 12-2-_3T is 2.8 (*Table 8*), and from five grains for sample P1B15-1_1T is 2.1 (*Table 10*) with an about 2.6.

4.4 Fracture Orientations

4.4.1 Transgranular Fracture Orientations

Equal-area, lower-hemisphere stereographic projection of the poles to open and sealed transgranular fractures, and shear transgranular fractures are shown for each sample with North plotted at top (Figures 10, 11, and 12). The different types of transgranular fractures generally show moderate to weak preferred orientations. The orientation of mesoscale faults measured by *Almeida* [2007] located within or near (< 1cm) the thin section is shown as red great circles in Figure 10, 11, and 12.

Shear transgranular fractures in each sample show the strongest preferred orientations that are similar to the nearest measoscale subsidary faults (Figure 10). The sample P1B11-1 does not contain any shear fractures (Figure 10a). Shear fractures are observed in all other samples (i.e., P1B13-1, P1B14-1, P1B16-2, and P1B17-4). The shear fractures in sample P1B13-1 display a strong preferred orientation. The fractures

22

are subvertical, strike northwest and are subparallel to the nearby mesoscale faults. The shear fractures in sample P1B14-1 also show a moderately strong preferred orientation. They dip steeply to the southeast, strike northeast, and form a moderate angle with the mesoscale faults. The shear fractures in sample P1B16-2 display a moderately strong preferred orientation, dip steeply to the southwest, strike southeast, and are subparalel mesoscale faults. The fractures in sample P1B17-4 have a preferred orientation and dip gently to moderately to the southwest, strike northwest, and are subparalel to the mesoscale faults. The composite plot of shear trasngranular fractures for all samples displays two moderately strong preferred orientations. The preferred orientation may represent either a diffuse point concentration or a conjugate pair with a large (greater than 45^0) dihedral angle. They dip steeply to southwest, strike northwest that are at a low angle to the SAF.

The orientation of mode 1 (open) fractures is generally dipping southwest, striking northeast, except for sample P1B11-1, which farthest from the SAF and the large subsidiary fault. P1B11-1 shows a diffuse point concentration (Figure 11a). The mode 1 (open) fractures in sample P1B13-1 display a strong preferred orientation. They are steeply dipping to the northeast, strike northwest and are subparallel to the mesoscale faults located near (< 1cm) the sample (Figure 11b). The mode 1(open) fractures in sample P1B14-1 show a moderate preferred orientation. They dip moderately from southwest to southeast and strike from northeast to southeast. They are oriented subparallel and at a moderate angle to the mesoscale faults located near the sample (Figure 11c). The mode 1(open) fractures measured from sample P1B16-2 displays a

strong preferred orientation and the poles to fractures define single point concentration (Figure 11d). Fractures dip steeply to southwest, striking northwest and are oriented at subparalel to the nearby mesoscale faults. The fractures in sample P1B17-4 shows a strong preferred orientation. They are moderately dipping to the southwest and strike northwest, similar to the fractures in sample P1B16-2 and P1B13-1 and they also form subparalel to nearby mesoscale faults. The composite plot of mode 1 (open) fractures for the all samples displays a strong preferred orientation (Figure 11e). The data show scatter, but generally dip approximately 30^0-40^0 to southwest, strike northwest; the average orientation is oriented at low angle to the SAF (Figure 11f).

The orientation of mode 1 (sealed) fractures is generally dipping southwest, striking northeast, except for sample P1B11-1, which farthest from the SAF and the large subsidiary fault and shows diffuse point concentration , not contoured (Figure 12a). The mode 1 (sealed) fractures in sample P1B13-1 display a strong preferred orientation. They are steeply dipping to the southwest, strike northwest and form moderate angle to the mesoscale faults located near (< 1cm) the sample (Figure 12b). The mode 1 (sealed) fractures in sample P1B14-1 show two different set preferred orientation. One set dip moderately southwest, and strike northeast, and form subparallel to the mesoscale faults located near the sample. The second set dips steeply southeast and strikes northeast, and form high angle to the mesoscale faults located near (< 1cm) the sample (Figure 12c). The mode 1(sealed) fractures measured from sample P1B16-2 displays a strong preferred orientation (Figure 12d). Fractures dip moderately to southwest, striking northwest and are oriented at subparallel to the nearby mesoscale faults (Figure 12d).

The fractures in sample P1B17-4 shows a strong preferred orientation. They are steeply dipping to the southwest and strike northwest. They also form subparallel to nearby mesoscale faults (Figure 12e). The composite plot of mode 1 (sealed) fractures for the all samples displays a strong preferred orientation. They dip moderately from southwest to southeast and strike from northeast to southeast. They are oriented subparallel and at a moderate angle to the SAF (Figure 12f).

When open, sealed, and shear transgranular fractures are combined for each sample, the preferred orientation varies from weak to strong preferred orientations (Figure 13). The transgranular fractures in sample P1B11-1 is not contoured and display diffuse point concentration. The fractures in sample P1B13-1 shows a strong preferred orientation. They are steeply dipping to northeast, strike northwest, and form subparallel to the mesoscale faults. The sample P1B14-1 displays a week preferred orientation. The fractures dip from south to northwest and strike northeast to southeast. The fractures in sample P1B16-2 display a strong preferred orientation and poles to fractures define a single point concentration. The fractures are steeply to moderately dipping to the southwest, strike northwest, and are oriented subparallel to the mesoscale faults. The fractures in sample P1B17-4 show a strong preferred orientation similar in orientation to sample P1B16-2; they dip steeply to moderately to the southwest, strike northwest, and are oriented approximately subparallel to the mesoscale faults. The composite plot for all trasngranular fractures (open, sealed, and shear) for the all samples displays a strong preferred orientation. Fractures generally dip southwest, strike northwest, and are subparallel to the SAF.

5. DISCUSSION

5.1 Quantifying Intragranular Linear Fracture Density in Healed Rocks

The linear fracture density in the arkosic sandstones from the western damage zone of the SAF gives representative measurements of fracture density for micro-scale deformation, at a particular distance from the main SAF core. The linear fracture densities are also analyzed in terms of proximity to important large subsidiary faults in this system. These data provide a critical estimate of fracture density for an active fault in the continental crust at seismogenic depths. The flat-stage traverse data increase our ability to determine relative fracture densities between samples and allow us to establish average fracture densities in different structural domains. The traverse technique, however, does sacrifice accuracy in defining the absolute magnitude of fracture density at a particular scale.

Previous studies of deformed sandstones have shown the importance of different imaging techniques to identify and characterize microfractures in minerals [e.g., Laubach, 1997]. This is particularly true for rocks deformed in the presence fluids at moderate temperatures, when given enough time to allow dissolution, diffusion and precipitation [e.g., *Brantley,* 1992; *Laubach*, 1988]. Given the previous work on the Phase 1 arkosic sandstone core, that documented significant petrographic and mineralogic evidence of diagenesis during faulting [e.g., *Chester et al.,* 2007; *Heron,* 2011], it is to be expected that sealing and healing of microfractures has been an important process in the damage zone of the SAF throughout the life of this fault. Taking these observations into account, standard microfracture studies of the arkosic sandstone

26

using low magnification optical microscopy techniques, as employed in the whole thin-section traverse technique, likely underdetermines the true microfracture density of these samples.

The dual SEM cathodoluminescence (CL) and plane-polarized-light (PPL) optical image analysis conducted on several grains in the sandstones is very successful at identifying a variety of fracture types. In general, this alternate technique reveals a significantly greater number of similar-size fractures, and leads to a greater linear fracture density estimate per grain. The increased fracture counts reflect the higher magnification and resolution of the digital images, which permits better crack identification. Nevertheless, these findings indicate that the higher resolution PPL optical microscopy alone, still underestimates fracture density. SEM-CL is particularly sensitive to different physical attributes, fracture shape, size, and cross-cutting relations [e.g., *Gomez and Laubach,* 2006]. Comparison of the fractures maps made from the SEM-CL and PPL microscopy images indicates that the majority of microfractures are resolved in both types of images. There are, however, a significant number of microfractures that are imaged only in SEM-CL, and to a lesser extent, only in PPL microscopy. This study illustrates, therefore, that both types of imaging is necessary to obtain a more accurate fracture density estimate of the sample, and that this combined imaging technique gives a substantially higher linear fracture density estimate when compared to the flat-stage whole-thin-section-traverse optical technique. On the basis of the handful of grains analyzed in the two petrographic sections for this study, the combined imaging produces fracture counts that are greater than those determined

through the whole-thin-section traverse technique by a factor of approximately 2.5 (*Tables 9 and 10*). This factor could be significant to understanding matrix permeability of reservoir systems over time, the evolution in physical properties of geologic systems, calculating fracture energy during earthquake rupture, and healing rates during interseismic periods [e.g., *Chester et al.,* 2005; *Wilson et al.,* 2005]. Although the advantages of using the SEM-CL technique are well documented [e.g. *Laubach*, 1997], to date no estimates of fracture energy have been corrected using this technique, and no estimate of a correction factor has been reported in the literature.

5.2 Scale Dependence of Fracture Density

The main purpose of the present work is to better evaluate whether fracturing in the damage zone of a large displacement, mature continental fault follows simple scaling laws, as has been inferred for fracturing in other settings [e.g., *Bonnet et al.,* 2001]. The detailed analysis of the SAFOD core allows quantification of fracture density at several scales of observation, as well as comparison to fracture density analyses at larger scales using borehole image logs.

The linear fracture density of the SAFOD Phase 1 arkosic sandstone core was determined at the mesoscopic scale by *Almeida* [2007, *written communication*, 2006]. Linear density was quantified by counting intercepts of fractures, deformation bands, and small gouge zones with a count line oriented parallel to the core axis. Intercepts were counted only for features that are continuous across the diameter of the core, i.e., features greater than 0.1 m in length. Such features were identified from wrap-around tracings of the outer core surface. On wrap-around maps of a cylindrical surface, the

trace of semi-planar features will produce sinusoidal patterns, so even though the trace of a fracture may not appear continuous across a wrap-around tracing, a continuous fracture can be confidently inferred if two or more traced segments are well fit by a sinusoid. In all, 104 features fit by sinusoids were mapped over the ~9 m of intact sections of the SAFOD Phase 1 arkosic sandstone core [*Almeida,* 2007]. For the section of the core comprised of pebbly sandstone, 3055.6 m MD (10025') to 3062.5 m MD (10047.6'), 79 intercepts were mapped, giving a fracture linear density of 11.4/m. Fracture density is variable, however, so the local mesoscopic scale fracture density was determined by the number of intercepts over a 0.6 m interval, centered on each sample location of the core (*Table 11*).

The mesoscopic scale linear fracture density of the same core was determined by B. Heron (*written communication,* 2009). In this work, fracture intercepts along count lines were acquired similar to the approach of *Almeida* [2007], except 10 evenly spaced count lines were used, and intercepts of all traced fractures, deformation bands and small gouge zones were counted. The smallest features mapped are approximately 0.01 m. In this sense, this work determines the linear density of all traced fractures greater in length than 0.01 m. For the section of the core comprised of pebbly sandstone, 3055.6 m MD (10025') to 3062.5 m MD (10047.6'), R.B. Heron (*written communication,* 2009) determined a linear density of *14.9/m* for a features excluding open fractures, and a linear density of *17.0/m* for all features including open fractures.

For purposes of estimating a cumulative linear density for fractures greater than a specific length, Almeida's estimate for fractures greater than 0.10 m length is preferred.

29

The work by *Heron* determines density for all fractures greater than ~0.01 m in length, but the values most likely are underestimated because of resolution issues.

The linear fracture density for grain-scale intragranular microfractures and transgranular fractures, from this study, are considered very robust as a result of measuring multiple representative samples and measuring three perpendicular sections from each sample. This approach circumvents problems associated with anisotropic fabrics and single directions of observation. In addition, the multiple techniques to determine intragranular microfracture counts, as described previously, combats undercounting due to resolution issues. The fracture densities and minimum fracture lengths defined for the mesoscopic scale data and the data for the two microscopic scales provided herein, produces three unique data points to evaluate the robustness of power-law relations between linear density and fracture-length in damage zones (*Table 12*; Figure 2).

In an effort to expand the range of scales considered, two more counts are included in the data set. The first count is also at the core scale, and focuses on the number of the largest subsidiary faults and on estimating the lengths of these features. Over the entire length of the Phase 1 arkosic sandstone core, including the lower sections comprised of fine-grained sandstone and siltstones, two significant subsidiary faults are present. These two faults, located at 3062 and 3067 m MD, are clearly more significant than all the other subsidiary faults captured in the core because they display well developed slip surfaces and thin gouge layers, as well as juxtapose different lithologic units, suggesting significant slip magnitudes. Given these two characteristics, the slip on

this fault category is hypothesized to be on the order of decimeters, and the lengths of these features greater than 5 m at a minimum.

To get a measure of fault density at the macroscopic scale, the results of the analysis by Draper-Springer of the SAFOD borehole west of the SDZ and east of the Buzzard Canyon fault is used [*Draper et al.,* 2009]. This section of the borehole is 1100 m in length and is contained within the arkosic sedimentary rock section, including the section cored during the Phase 1 drilling at SAFOD. *Draper et al.* [2009] studied borehole image logs to determine bedding orientations over the 1100 m section. They document that the sedimentary unit is cut by 11 faults forming blocks with uniform strikes and dips. The blocks range from tens to two hundred meters in thickness. These characteristics are taken as evidence that significant slip occurred on the faults identified by *Draper et al.* [2009]. It is not unreasonable to infer that the length of the faults is at least equivalent to the length of the bocks; the minimum length of the eleven faults is estimated as 50 m.

These two macroscopic scale estimates are significantly less certain than those made at the smaller scales because of the minimal sampling volume and uncertainty in minimum length of the counted faults. Nonetheless, these additional measurements are useful for purposes of comparison with the mesoscopic and microscopic scale data. The various scales of observation, sampled area or volumes, minimum length of the counted fractures and subsidiary faults, and calculated liner densities are provided in *Table 12*. The tabulated values are shown in a log-log plot of linear density versus feature length in Figure 14. In spite of the uncertainty in values at the longer length scales, the data

clearly are consistent with a linear relation, and are well described by a power-law

scaling function. Actually, the result is not too sensitive to the length estimates for the

two macroscopic data points; to produce a significant deviation from the observed

relationship would require changing the length by a factor of 10 or more, and such

values are extremely unlikely given the nature of the deformation features.

5.3 Similarity of Fracture Distribution at SAFOD and the Punchbowl Fault

The Punchbowl fault is an inactive strand of the SAF that has been exhumed

approximately 2-4 km. [*Chester and Logan*, 1986]. Therefore, the fracture distribution

within the damage zone of the exhumed fault of the SAF such as the Punchbowl Fault

with the data from the Phase 1 arkosic sandstone of the SAF at SAFOD documented

herein can be compared consistently.

The transgranular fracture density of the Phase 1 arkosic sandstone core

[*Almeida, unpublished data,* 2007] as a function of distance (~100 m) from the SDZ of

the SAF is compared to the density versus log distance relationship determined for

subsidiary faults in the damage zone of the Punchbowl Fault on a linear density versus

distance from the fault graph (Figure 15).According to this graph, data are seen on the

same best fit line suggesting that microscale fracture density (trangranular fracture

density) from the arkosic sandstone of the SAF at SAFOD is compatible with mesoscale

fracture density (subsidiary fault) from the arkosic sandstone of the Punchbowl Fault so

fracture distribution of two sandstone is similar.

Figure 15 shows consistency of fracture densities of the two sandstones (SAF

and Punchbowl Fault) at different scales (micro- and meso-scale). In addition to this

observation, density values of the two sandstones at the same scale are compared (Figure 16). Intragranular density values of the arkosic sandstone from SAFOD Phase 1 core are documented using two different techniques: the whole thin section traverse technique and imaging technique based on correction of SEM-CL and optical images. Intragranular fracture density of the Phase 1 arkosic sandstone core as a function of distance (~100 m) from the SAF, SDZ compared to the density versus log distance relationship determined for intragranular microfractures in the damage zone of the Punchbowl Fault on the linear density versus distance from the fault graph Figure 16. The intragranular fracture density determined using the whole thin section traverse technique falls below the intragranular fracture density determined using correction factor derived from the SEM-CL-Optical fracture density analysis.

5.4 Scale Dependence of Fracture Orientation

The scale dependence of the fabric in the damage zone is addressed by comparison of transgranular fracture fabrics with the mesoscale subsidiary fault fabric (Figure 17). Overall, transgranular fractures display a diffuse but preferred orientation approximately parallel to the dominant set of the subsidiary faults. This is consistent with the expectation that transgranular fractures are dominantly shear fractures, and thus should be similar in orientation to mesoscale faults. The poles to shear transgranular fractures show strong point concentration for all samples. In fact, none of the fracture distributions indicates that shear fractures formed conjugate sets (Figure 10). However, when the data from all samples combined, the preferred orientation displays either a diffuse point concentration or a conjugate sets. The poles to mode 1(open) transgranular

fractures are not compatible with mesoscale fracture fabric. The mode 1 (sealed) trasngranular fractures are compatible with mesoscale fracture fabric, but there is not much data to make statistical analysis for mode 1 (sealed) fractures. Thus orientation distribution data for subsidiary faults and transgranular fractures are consistent with fabric invariance between the microscale and mesoscopic scale. It is not, however, expected that transgranular fractures and intragranular fractures, particularly in granular aggregates, would be the same. This idea was not tested in the present work.

6. CONCLUSIONS

Combined use of SEM-CL and PPL microscopy image analysis improves the accuracy of estimates of linear fracture density at the grain scale.

Linear fracture density in the damage zone of the SAF at SAFOD follows a simple power-law scaling relation over the grain scale to km scale range.

The fabric of transgranular microscopic fractures measured at the whole-thin section scale is similar to that of mesoscopic scale subsidiary faults. A test of the similarity in fabric between the transgranular and intragranular scales was not completed.

The densities and orientation distributions of fractures in the damaged arkosic sandstone of the SAF at SAFOD is similar to that observed in the arkosic sandstone of the Punchbowl Fault (an ancient exhumed trace of the San Andreas system) suggesting that the scaling relationship determined may be general applicability.

REFERENCES

Almeida, R. (2007), Mesoscale fracture fabric and paleostress along the San Andreas
Fault at SAFOD, M.S. thesis, Department of Geology and Geophysic, Texas
A&M University, College Station, TX.

Anders, M.H. and D.V. Wiltschko (1993), Microfracturing, paleostress, and the growth
of faults, *Journal of Structural Geology, 16*, 795–815.

Bailey, E.H. and R.E. Stevens (1960), Selective staining of K-feldspar and plagioclase
on rock slabs and thin sections*, American Mineralogist, 45*, 1020-1025.

Boness, N. and M. Zoback (2006), A multi-scale study of the mechanisms controlling
shear velocity anisotropy in the San Andreas Fault Observatory at Depth,
Geophysics, 71 (5), F131-F146.

Bonnet, E., O. Bour, N.E. Olding, P. Davy, I. Main, P. Cowie, and B. Berkowitz (2001),
Scaling of Fracture Systems in Geological Media, *Reviews of Geophysics*, *39*,
347-383.

Bradbury, K.K., D.C. Barton., S.D. Draper, J.G. Solum, and J.P. Evans (2007),
Mineralogic and textural analyses of drill cuttings from the San Andreas Fault
Observatory at Depth (SAFOD) boreholes: Initial interpretations of fault zone
composition and constraints on geologic models, *Geosphere, 3*, 299–318, doi:
10.1130/GES00076.1.

Brantley, S.L. (1992), The effect of fluid chemistry on quartz microcrack lifetimes,
Earth and Planetary Science Letters, 113, 145–156.

Caine, J.S., J. P. Evans, and C. B. Forster (1996), Fault zone architecture and

permeability structure, *Geology, 24*, 1025-1028, doi:10.1130/0091-7613(1996)024<1025:FZAAPS>2.3.CO;2.

Catchings, R. D., M. J. Rymer, M. R. Goldman, J. A. Hole, R. Huggins, and C. Lippus (2002), High-resolution seismic velocities and shallow structure of the San Andreas Fault zone at Middle Mountain, Parkfield, California, *Bulletin of the Seismological Society America, 92,* 2493-2503.

Chester, F.M. and J.S. Chester (1998), Ultracataclasite structure and friction processes of the San Andreas Fault, *Tectonophysics, 295*, 199-221.

Chester, F. M. and J. Logan (1986), Implications for mechanical properties of brittle faults from observations of the Punchbowl Fault zone, California, *Pure and Applied Geophysics, 124*, 79-106.

Chester, F.M., J.P. Evans., and R.L. Biegel (1993), Internal structure and weakening mechanisms of the San-Andreas fault, *Journal of Geophysical Research Solid Earth, 98* (B1), 771-786.

Chester, F.M., J.S. Chester, D. Kirschner, S. Schulz, and J.P. Evans (2004), Structure of large-displacement fault zones in the brittle continental crust, *Rheology and Deformation in the Lithosphere at Continental Margins*, 1-42.

Chester, J.S. (2011). Personal Communication.

Chester, J S. and F M. Chester (2006), Energy Dissipation and Damage Generation in Seismic Fault Zones, *Eos Transaction American Geophysical Union, 87*(52), Fall Meeting Supplement., Abstract T31FF-05 Invited.

Chester, J. S., F. M. Chester, and A. K. Kronenberg (2005), Fracture surface energy of

the Punchbowl fault, San Andreas system, *Nature, 437*(7055), 133-136, doi:10.1038/nature03942.

Chester, J.S., F.M. Chester, D.L. Kirschner, R. Almeida, J.P. Evans, R.N. Guillemette, S. Hickman, M. Zoback, and W. Ellsworth, (2007), Deformation of sedimentary rock across the San Andreas Fault Zone: Mesoscale and microscale structures displayed in core from SAFOD, *Eos,Transactions of the American Geophysical Union. 88*(52), Fall Meeting Supplement, Abstract T42C-05.

Cornet, F.H., P. Bernard, and I. Moretti (2004), The Corinth Rift Laboratory. Comptes Rendus *Geoscience, 336*, 235–241, doi:10.1016/ j. crte.2004.02.001.

Dickinson, W.L. (1970), Interpreting Detrial Modes of Graywacke and Arkose, *Journal of Sedimentary Petrology, 40*, 2, 695-707.

Dor, O., J.S. Chester, Y. Ben-Zion, J.N. Brune, and T. K. L. Rockwell (2009), Characterization of Damage in Sandstones along the Mojave Section of the San Andreas Fault: Implications for the Shallow Extent of Damage Generation, *Pure and Applied Geophysic,* 166, 1747-1773.

Draper S., S., Evans, J.P., Garver, J.I., Kirschner D., and Janecke, S.U. (2009), Arkosic rocks from the San Andreas Fault Observatory at Depth (SAFOD) borehole, central California: Implications for the structure and tectonics of the San Andreas Fault zone. *Lithosphere, 1*(4), 206-226; doi: 10.1130/L13.1

Faulkner, D. R., C. A. L. Jackson, R. J. Lunn, R. W. Schlische, Z. K. Shipton, C. A. J. Wibberley, and M. O. Withjack (2010), A review of recent developments concerning the structure, mechanics and fluid flow properties of fault zones,

Journal of Structural Geology, 32, 1557–1575, doi:10.1016/j.jsg.2010.06.009.

Faulkner, D. R., T. M. Mitchell, E. Jensen, and J. Cembrano (2011), Scaling of fault damage zones with displacement and the implications for fault growth processes, *Journal of Geophysical Research, 116*(B5), doi: 10.1029/2010jb007788.

Friedman, M. (1969), Structural Analysis of Fractures in Cores from Saticoy Field, Ventura County, California, *The American Association of Petroleum Geologist Bulletin*, *53*(2), 367-389.

Gabriel, A. and E. P. Cox (1929), A staining method for the quantitative determination of certain rock minerals, *American Mineralogist, 14*, 290-292.

Gomez, L.A., and S.E. Laubach (2006), Rapid digital quantification of microfracture populations, *Journal of Structural Geology 28*, 408-420.

Heron, B. (2011), Grain-scale Comminution and Alteration of Arkosic Rocks in the Damage Zone of the San Andreas Fault at SAFOD, M.S. thesis, Department of Geology and Geophysic, Texas A&M University, College Station, TX.

Heron, B. (2009). Written Communication.

Hickman, S., M. Zoback, and W. Ellsworth (2004), Introduction to special section: Preparing for the San Andreas Fault Observatory at Depth, *Geophysical Research Letters, 31*, L12S01, doi:10.1029/2004GL020688.

Holdsworth, R.E., E.W.E. van Diggelen, C.J. Spiers, J.H.P. de Bresser, R.J. Walker, and L. Bowen (2011), Fault rocks from the SAFOD core samples: Implications for weakening at shallow depths along the San Andreas Fault, California, *Journal of Structural Geology, 33*(2), 132-144.

Imber, J., R. E. Holdsworth, S.A.F. Smith, S. P. Jefferies, and C. Collettini (2008), Frictional-viscous flow, seismicity and the geology of weak faults: A review and future directions, *Geological Society, London Special Publication, 299*, 151-173.

Laubach, S. E. (1988), Subsurface fracture and their relationship to stress history in East Texas basin sandstone, *Tectonophysics, 156,* 37-49.

Laubach, S. E. (1997), A method to detect natural fracture strike in sandstone, *Association of American Petroleum Geologists Bulletin, 81*, 4, 604-623.

Ma, K. F., H. Tanaka, S. R. Song, C.Y. Wang, J.H. Hung, Y.-B. Tsai, J. Mori, Y.F. Song, E.C. Yeh, W. Soh, H. Sone, L.W. Kuo, and H.Y. Wu (2006), Slip zone and energetics of a large earthquake from the Taiwan Chelungpu-fault Drilling Project, *Nature, 444*, 473-476, doi:10.1038/nature05253.

Milliken, K.L. and S.E. Laubach (2000), Brittle deformation in sandstone diagenesis as revealed by scanned cathodoluminescence imaging with application to characterization of fractured reservoirs, in Cathodoluminescence in Geoscience, edited by Pagel, M. et al., *Springer, Berlin,* 225-243.

Mitchell, T.M. and D.R. Faulkner (2009), The nature and origin of off-fault damage surrounding strike-slip fault zones over a wide range of scales: A field study from the Atacama fault zone, northern Chile, *Journal of Structural Geology, 31*(8), 802-816.

Mitchell, T.M. and D.R. Faulkner (2012), Towards quantifying the matrix permeability of damage zones in low porosity rocks, *Earth and Planetary Science Letters*, 339-340.

Neal, A. L. (2002), Internal Structure of the Kern Canyon Fault, California. M.S. thesis, Department of Geology and Geophysic, Texas A&M University, College Station, TX.

Ohtani, T., H. Tanaka, K. Fujimoto, T. Higuchi, N. Tomida, and H. Ito (2001), Internal structure of the Nojima Fault zone from the Hirabayashi GSJ drill core, *The Island Arc, 10*, 392, doi: 10.1046/ j.p1440–1738.2001.00337.x.

Savage, H. M. and E. E. Brodsky (2011), Collateral damage: Evolution with displacement of fracture distribution and secondary fault strands in fault damage zones, *Journal of Geophysical Research, 116*, B03405, doi:10.1029/2010JB007665.

Savage, J. C. and R. O. Burford (1971), Discussion of paper by C. H. Scholz and T. J. Fitch, "Strain accumulation along the San Andreas Fault", *Journal of Geophysical Research, 76*, 6469-6479.

Scholz, C. (2000), Evidence for a strong San Andreas Fault, *Geology, 28*, 163-166.

Schulz, S.E. and J.P. Evans (1998), Spatial variability in microscopic deformation and composition of the Punchbowl fault, southern California: Implications for mechanisms, fluid-fault interaction and fault morphology, *Tectonophysics,* 295, 223-244.

Schulz, S. E. and J. P. Evans (2000), Mesoscopic structure of the Punchbowl Fault, Southern California and the geologic and geophysical structure of active strike-slip faults, *Journal of Structural Geology*, 22, 913-930.

Solum, J. G., S. H. Hickman, D. A. Lockner, D. E. Moore, B. A. van der Pluijm, A. M. Schleicher, and J. P. Evans (2006), Mineralogical characterization of protolith and fault rocks from the SAFOD Main Hole, *Geophysical Research Letter, 33*(21), doi:10.1029/2006gl027285.

Takagi H., T. Kazuhiro, S. Koji, T. Kosuke, M. Reiko, K. Narumi, and T. Shigeru (2012), Transport Phenomena during the Fast Filling Process in a Hydrogen Tank for the Fuel Cell Vehicle, *Journal of Advanced Research in Physics, 3*, 1

Titus, S., C. DeMets, and B. Tikoff (2006), Thirty-five-year creep rates for the creeping segment of the San Andreas Fault and the effects of the 2004 Parkfield earthquake: constraints from alignment arrays, continuous global positioning system, and creepmeters, *Bulletin of Seismological Society of America, 96*, 250-268. doi:10.1785/0120050811.

Tobin, H.J. and M. Kinoshita (2006), Investigations of seismogenesis at the Nankai Trough, Japan, *Integrated Ocean Drilling Program Scientific Prospectus*, NanTroSEIZE Stage 1. doi:10.2204/iodp.sp.nantroseize1.

Wallace, R.E. and H.T. Morris (1986), Characteristics of faults and shear zones in deep mines, *Pure and Applied Geophysics, 124*, 107-125.

Wilson, B., T. Dewers, Z. Reches, and J. Brune, (2005), Particle size and energetics of gouge from earthquake rupture zones, *Nature, 434*, 749-752.

Wilson, J., J.S. Chester, and F.M. Chester (2003), Microfracture fabric of the Punchbowl Fault zone, San Andreas system, California, *Journal of Structural Geology, 25*, 1856-1873.

Zoback, M., H. Hickman, and W. Ellsworth (2006), Structure and properties of the San Andreas fault in central California: Preliminary results from the SAFOD experiment. *Geophysical Research* Abstract, 8:02474.

Zoback, M.D., S. Hickman, and W. Ellsworth (2007), The role of fault zone drilling, 2007, In Kanamori, H., and Schubert, G. (Eds.), Earthquake Seismology - Treatise on geophysics. Amsterdam, The Netherlands (Elsevier), in press.

Zoback, M., S. Hickman, and W. Ellsworth (2010), Scientific drilling into the San Andreas fault zone, *Eos Transaction American Geophysical Union, 91*(22), 197-199.

Zoback, M., S. Hickman, and W. Ellsworth (2011), Scientific Drilling Into the San Andreas Fault Zone – An Overview of SAFOD's First Five Years, *Scientific Drilling*, doi: 10.2204/iodp.sd.11.02.2011.
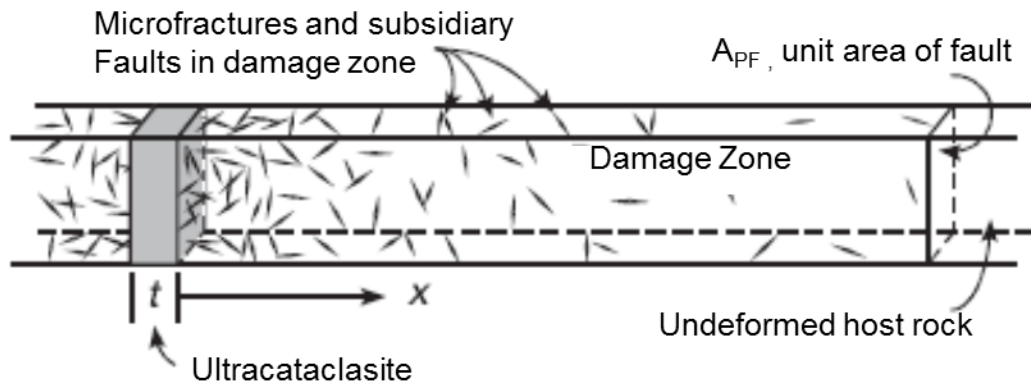
Figure 1. Common fault zone structure [From *Chester et al.*, 2005].
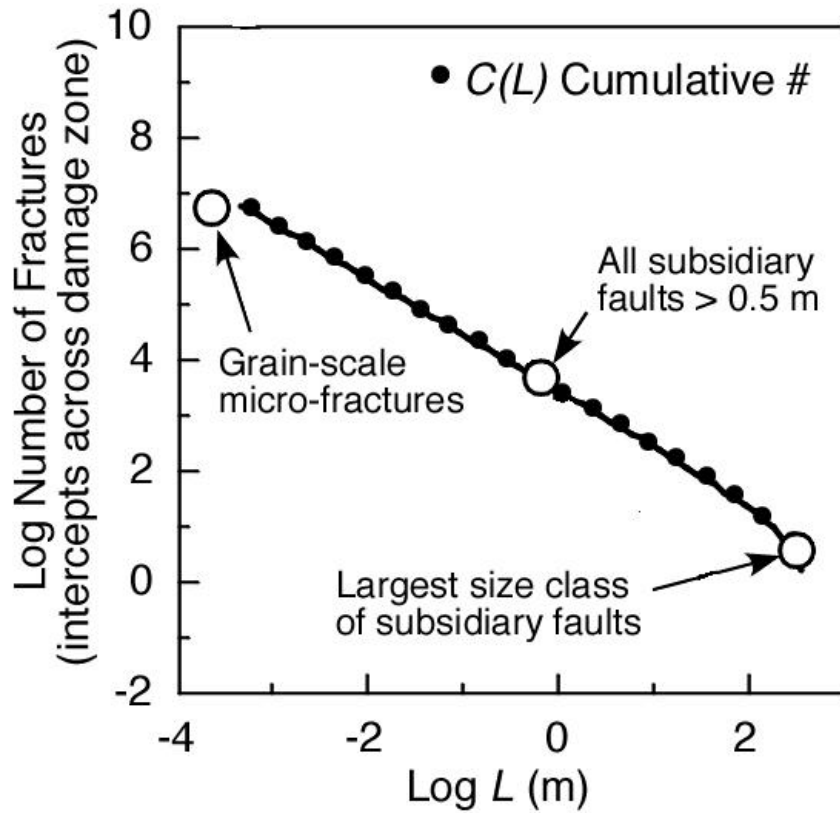
Figure 2. Total number of fractures as a function of fracture length, L, for the Punchbowl Fault Damage Zone in the Punchbowl Formation arkosic sandstone at the Devil's Punchbowl County Park, California. Total number of fractures is the number intercepted by a count line oriented perpendicular to the fault. The average fracture density (#/m) can be determined by dividing the total number by the thickness of the damage zone, ~100 m. This plot, reported in Chester and Chester [2006], is based on data reported by Wilson et al., [2003], and plotted and analyzed by Chester et al. [2005]. This result suggests that the relation between fracture density and fracture length follows a power-law because the data appears to follow a linear relation in log-log space.
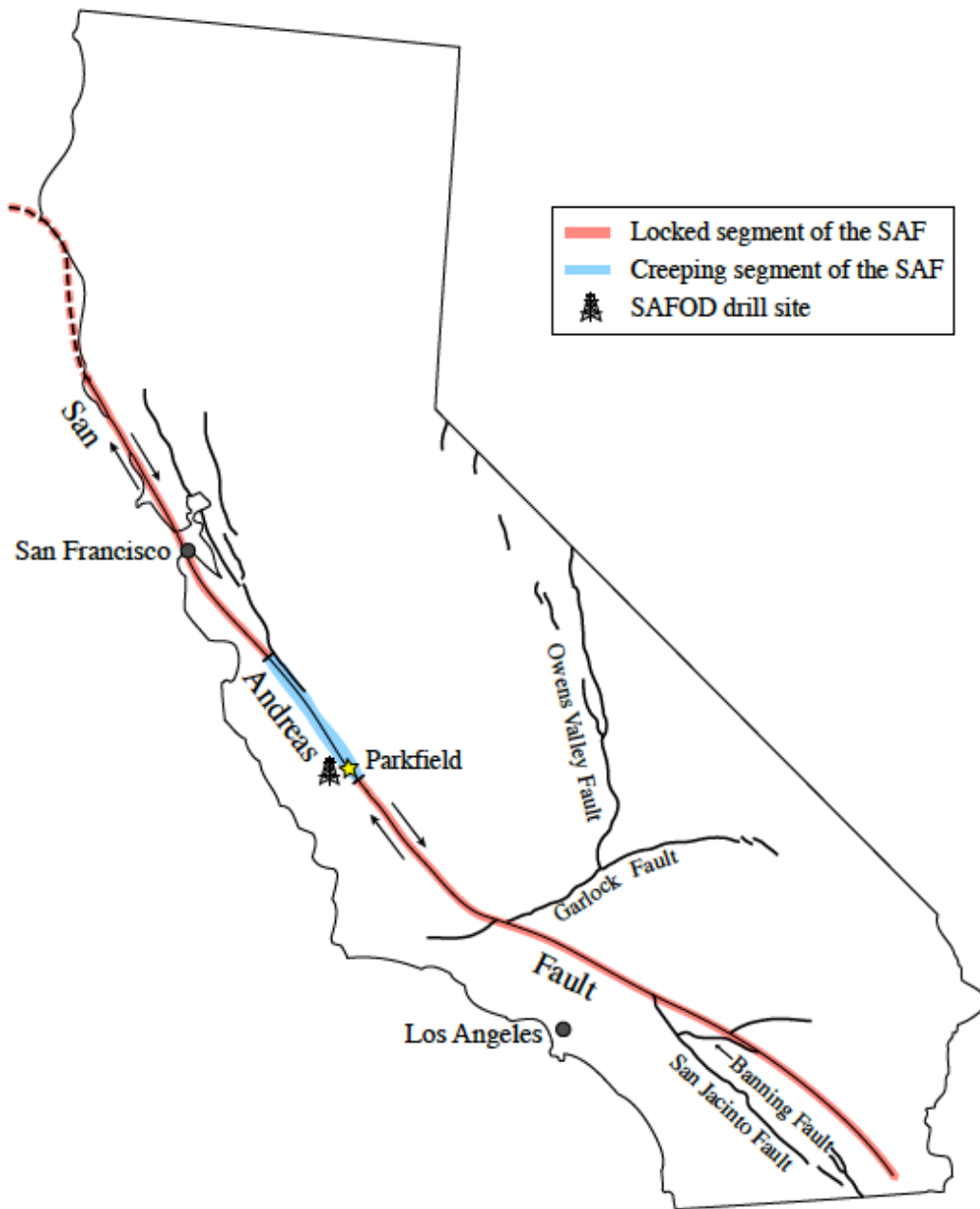
Figure 3. Map of California showing locations of the northern and southern locked segments and the central creeping segment of the San Andreas Fault as well as the location for the SAFOD drill site [From *Heron*, 2011].

46
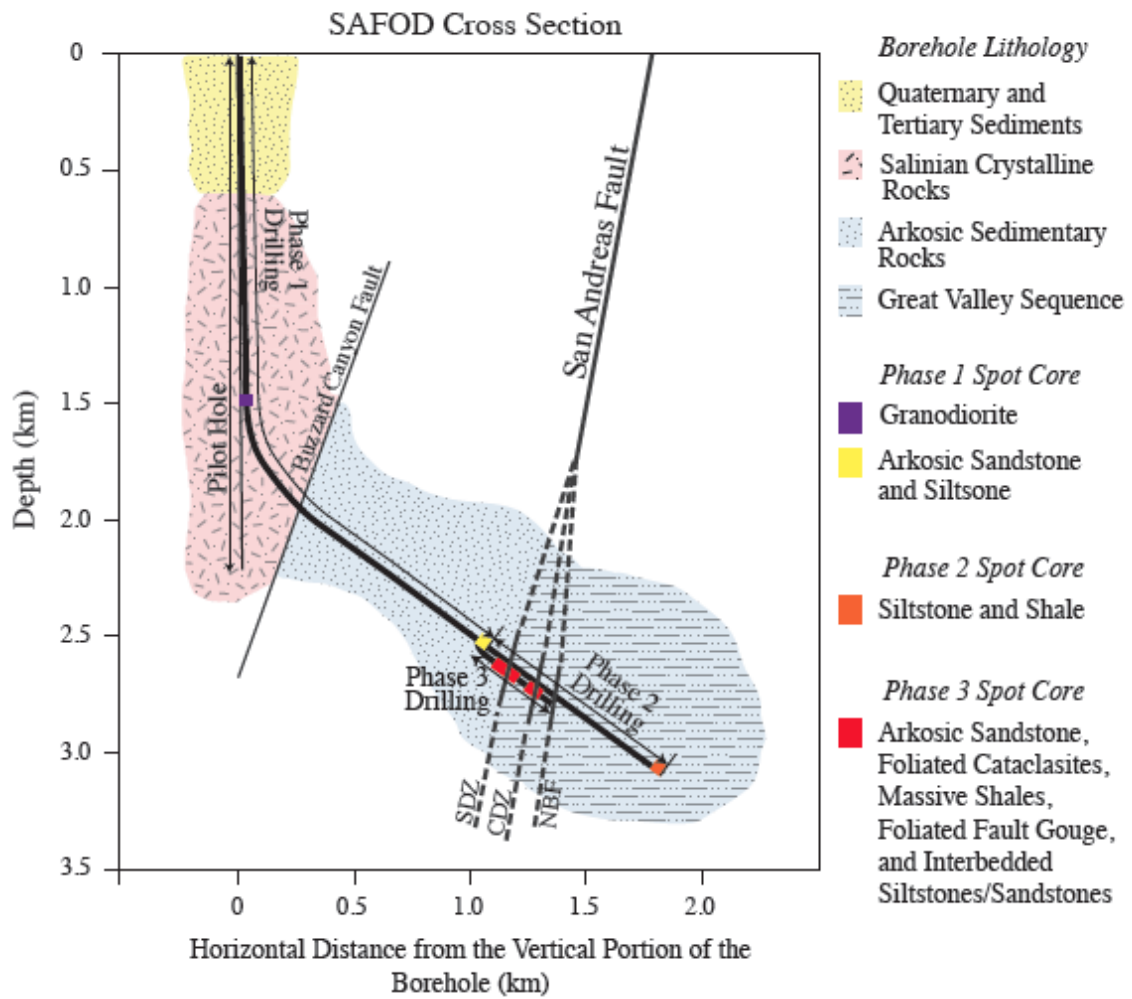
Figure 4. Cross section is indicating the SAFOD borehole, borehole lithology, and spot cores taken during the Phase 1, Phase 2, and Phase 3 drillings [From Heron, 2011].
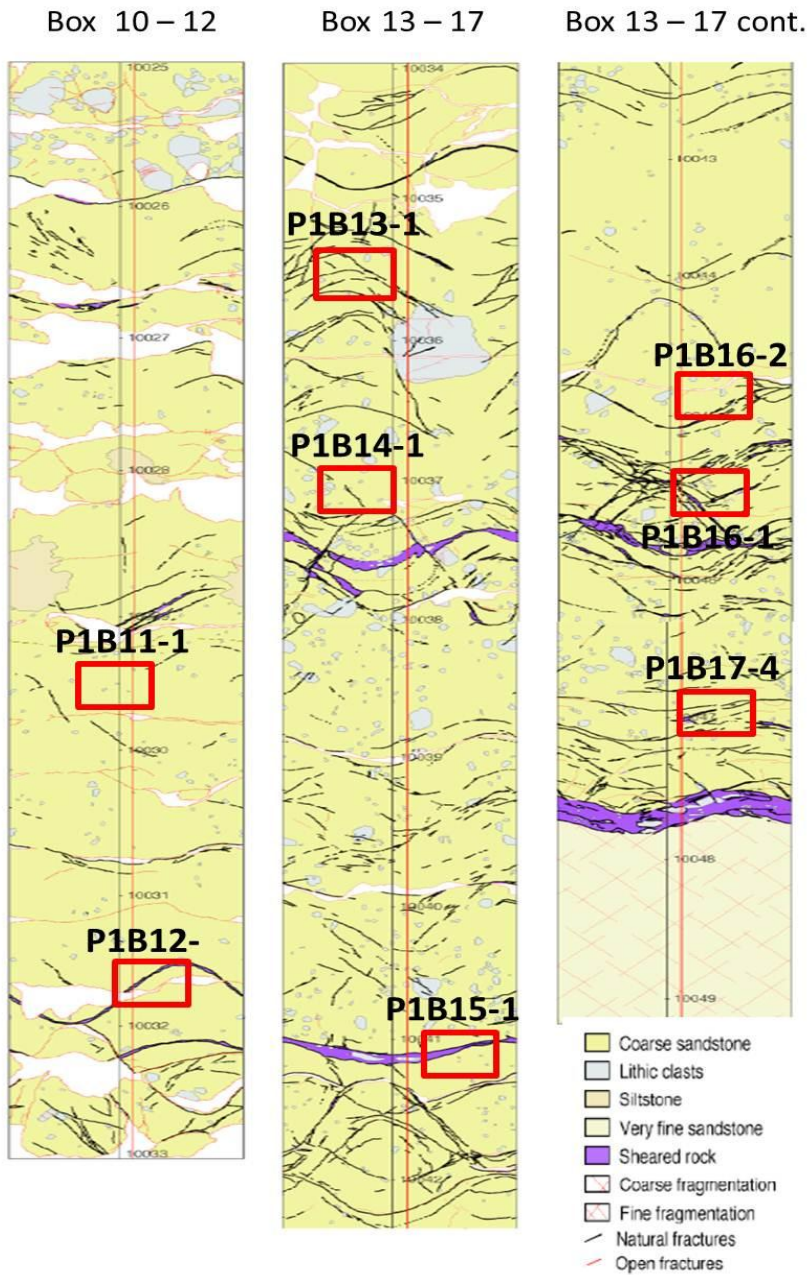
Figure 5. Wrap around maps of the arkosic sandstone, siltstone, and shale spot core from Phase 1, showing the locations of the samples used in this study (red boxes), and mesoscale faults plotted in later figures (green sinusoids). The wrap-around maps were made at the SAFOD drill site by J.S. Chester and F. M. Chester. This is a slightly modified version of the maps that were presented in Almeida [2007] and Heron [2011].

a. PLL image   b. XPL image
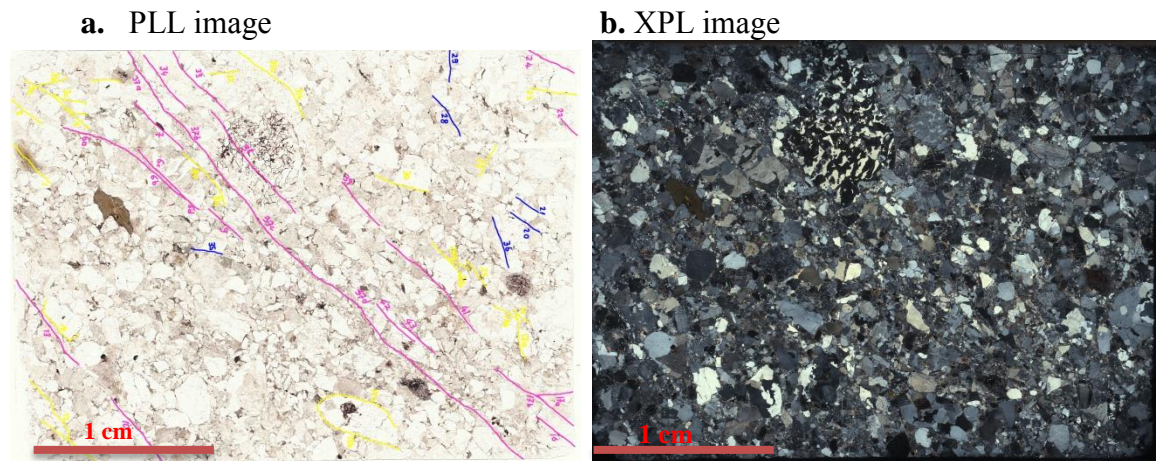
Figure 6. Representative map of transgranular fractures for one petrographic thin section (P1B13-1-2T). (a) Transgranular fractures are shown on top of the plane polarized image (PPL) of the thin section. (b) Cross polarized image (XPL) of the same thin section.
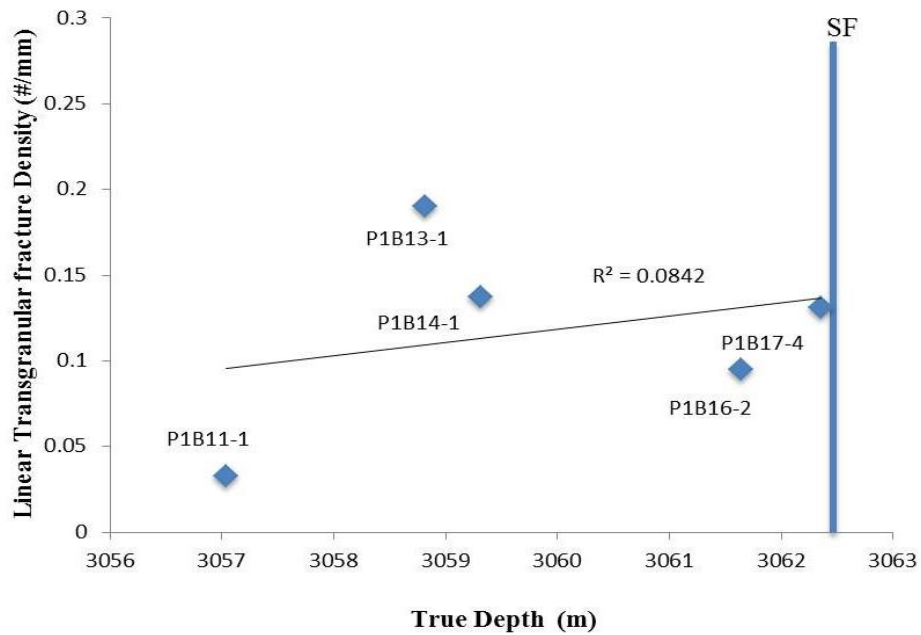
Figure 7. Linear transgranular fracture density variation relative to distance from the large mesoscale subsidiary fault (SF, blue line) located at 3062.5 m MD shown in the wrap-around maps of the Phase 1 core (Figure 5).
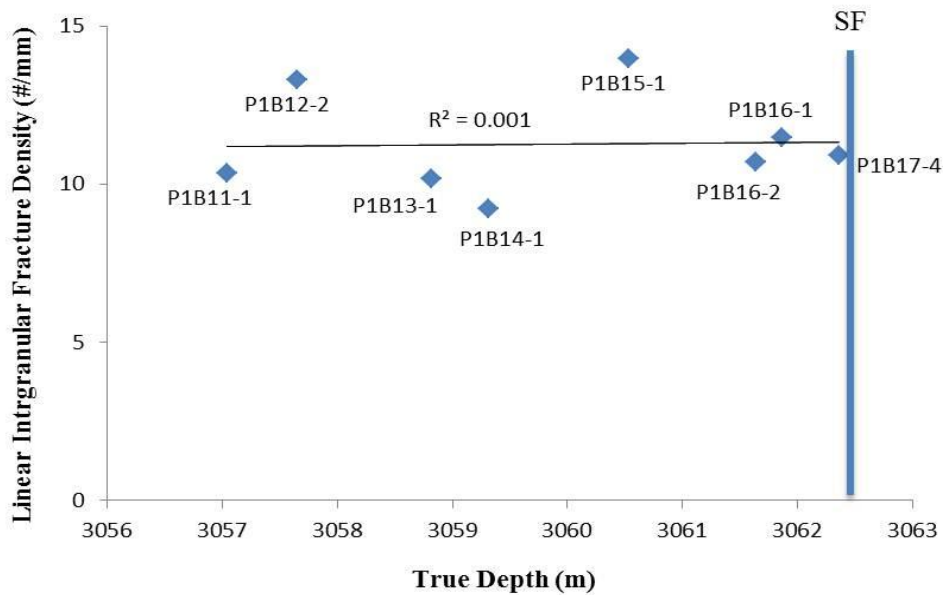
Figure 8. Linear intragranular fracture density variation relative to distance from the large mesoscale subsidiary fault (SF, blue line) located at 3062.5 m MD shown in the wrap-around maps of the Phase 1 core (Figure 5).

50
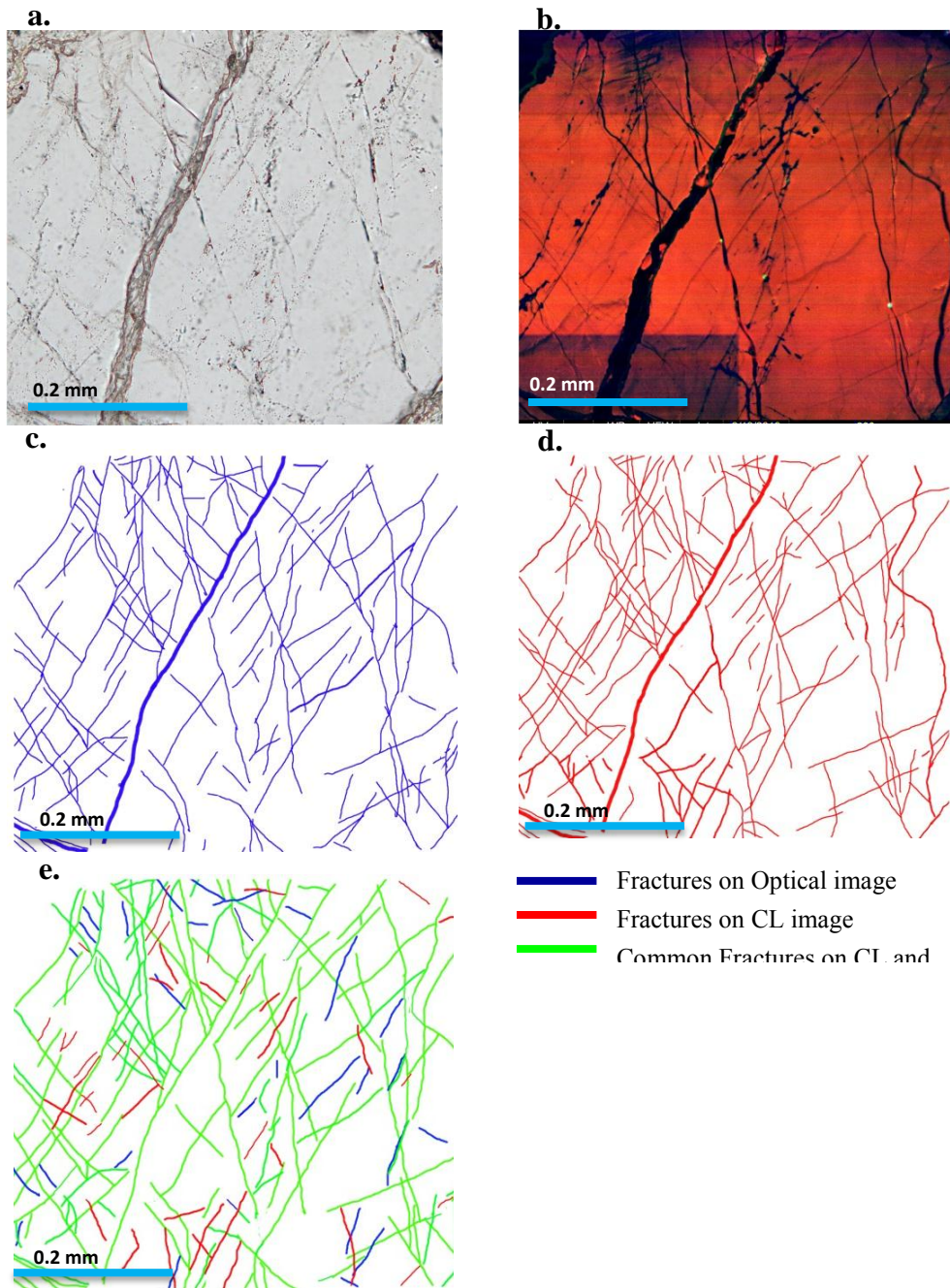
Figure 9. Representative optical and SEM-CL images and intragranular fracture maps for one grain used to determine the intragranular linear fracture density correction factor. All data shown are for Grain 3 from P1B12-2_3-T. (a) Optical image taken under plane polarized light; (b) SEM-CL image; (c) Intragranular fracture map for optical image; (d) intragranular fracture map for SEM-CL image; (e) Composite map showing fractures observed with both imaging techniques.

Shear Transgranular Fracture Orientations
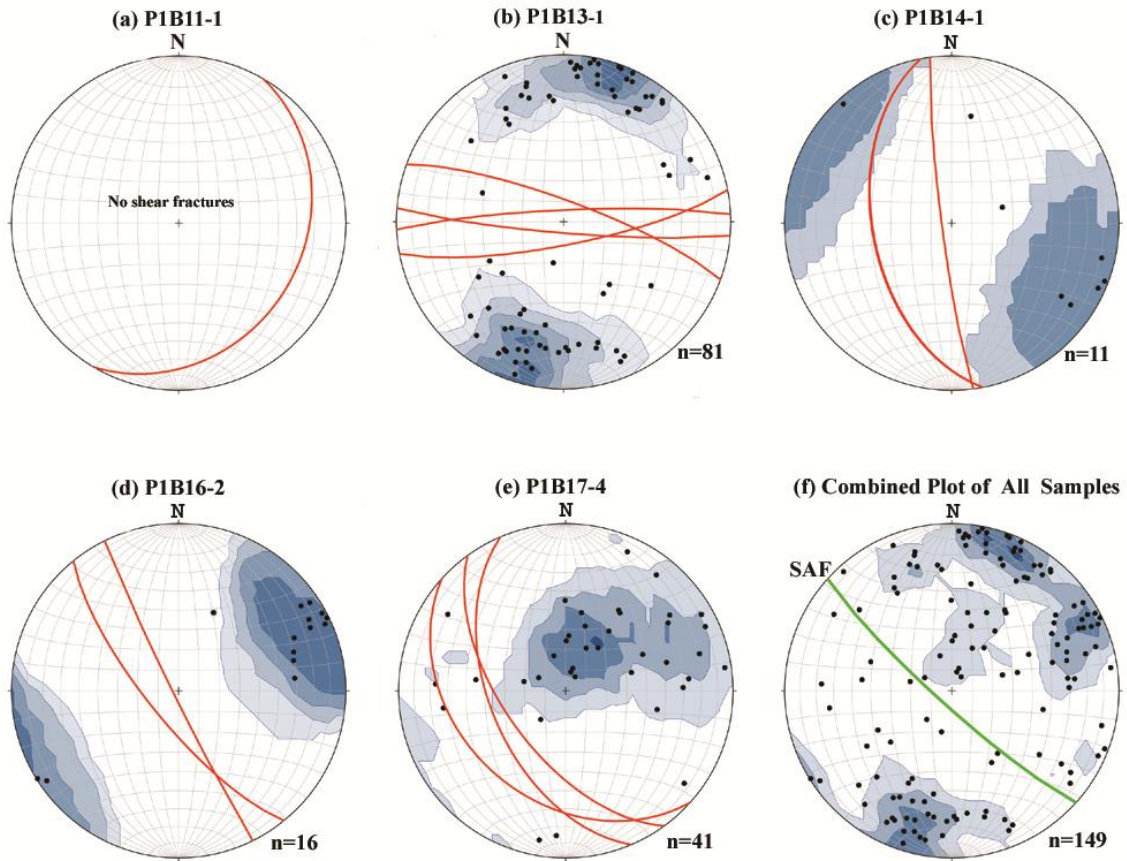
Figure 10. Orientation of transgranular shear fractures cutting the Phase 1 arkosic sandstone. Poles to fractures are plotted in a lower hemisphere equal-area projection with North (N) at top. Data are contoured with a two sigma contour interval, using the Kamb method and OSXStereonet v. 1.7 by N. Cardozo and R. Allmendinger [2011]. The planes of mesoscale faults that cut the samples or that are nearby are shown as red great circles (n=number of fractures).Data plotted for samples (a) P1B11-1; (b) P1B13-1; (c) P1B14-1; (d) P1B16-2; (e) P1B17-4; (f) Combined data from slides P1B13-1, P1B14-1, P1B16-2, P1B17-4.

52
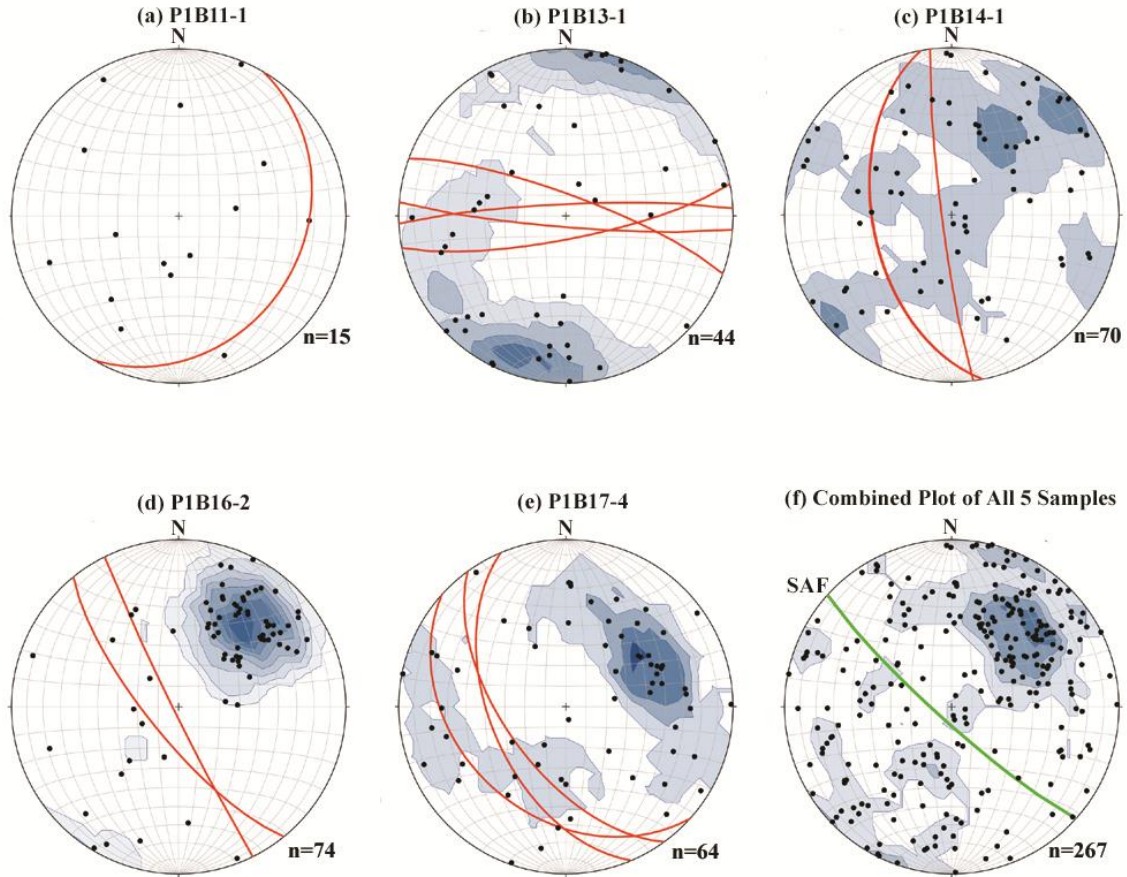
Figure 11. Orientation of transgranular open fractures cutting the Phase 1 arkosic sandstone. Poles to fractures are plotted in a lower hemisphere equal-area projection with North (N) at top. Data are contoured with a two sigma contour interval, using the Kamb method and OSXStereonet v. 1.7 by N. Cardozo and R. Allmendinger [2011]. The planes of mesoscale faults that cut the samples or that are nearby are shown as red great circles (n=number of fractures). Data plotted for samples (a) P1B11-1; (b) P1B13-1; (c) P1B14-1; (d) P1B16-2; (e) P1B17-4; (f) Combined data from slides P1B13-1, P1B14-1, P1B16-2, P1B17-4.

Mode 1 (Sealed) Fracture Orientations

(a) P1B11-1

(b) P1B13-1

(c) P1B14-1

(d) P1B16-2

(e) P1B17-4

(f) Combined Plot of All 5 Samples

n=7, n=21, n=45, n=11, n=8, n=92
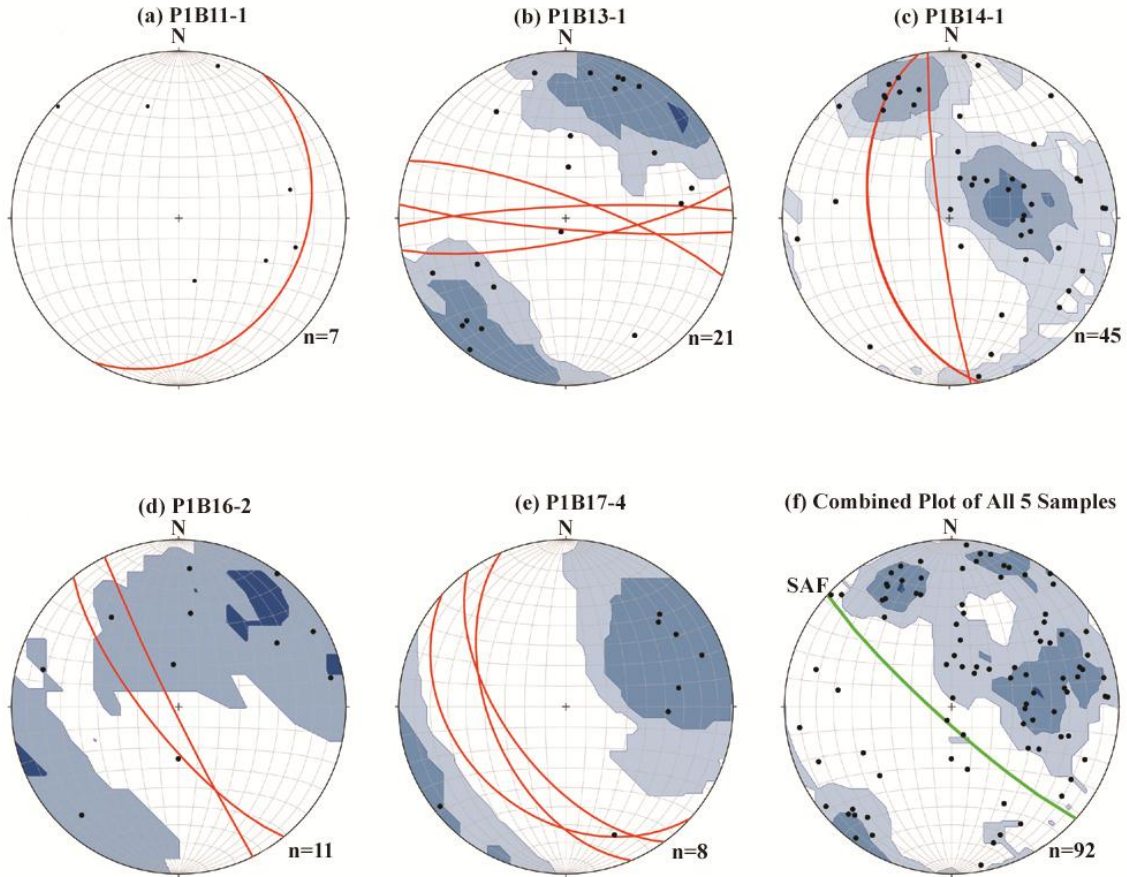
Figure 12. Orientation of transgranular sealed fractures cutting the Phase 1 arkosic sandstone. Poles to fractures are plotted in a lower hemisphere equal-area projection with North (N) at top. Data are contoured with a two sigma contour interval, using the Kamb method and OSXStereonet v. 1.7 by N. Cardozo and R. Allmendinger [2011]. The planes of mesoscale faults that cut the samples or that are nearby are shown as red great circles (n=number of fractures). Data plotted for samples (a) P1B11-1; (b) P1B13-1; (c) P1B14-1; (d) P1B16-2; (e) P1B17-4; (f) Combined data from slides P1B13-1, P1B14-1, P1B16-2, P1B17-4.

The Orientation of Transgranular Fractures

(a) P1B11-1

(b) P1B13-1

(c) P1B14-1

(d) P1B16-2

(e) P1B17-4

(f) Combined Plot of All 5 Samples
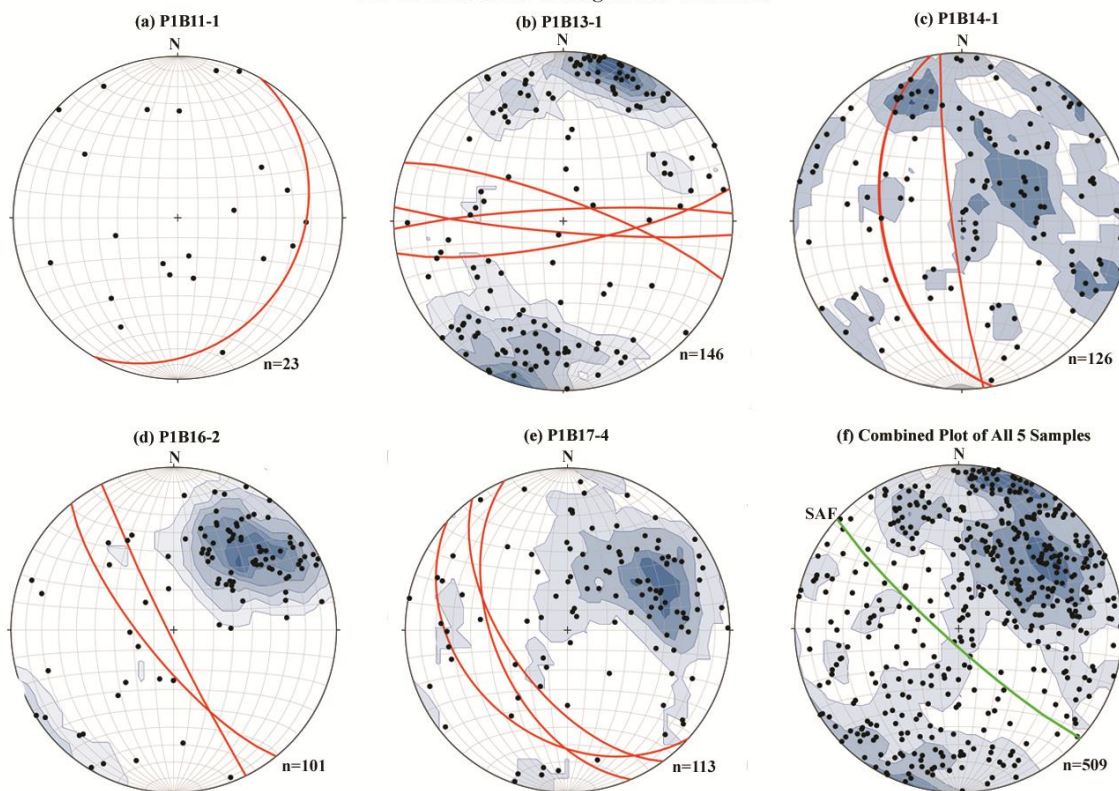
Figure 13. Orientation of all transgranular fractures cutting the Phase 1 arkosic sandstone. Poles to fractures (black dots) are plotted in a lower hemisphere equal-area projection with North (N) at top. Data are contoured with a two sigma contour interval, using the Kamb method and OSXStereonet v. 1.7 by N. Cardozo and R. Allmendinger [2011]. The planes of mesoscale faults that cut the samples or that are nearby are shown as red great circles (n=number of fractures). Data plotted for samples (a) P1B11-1; (b) P1B13-1; (c) P1B14-1; (d) P1B16-2; (e) P1B17-4; (f) Combined data from slides P1B13-1, P1B14-1, P1B16-2, P1B17-4.
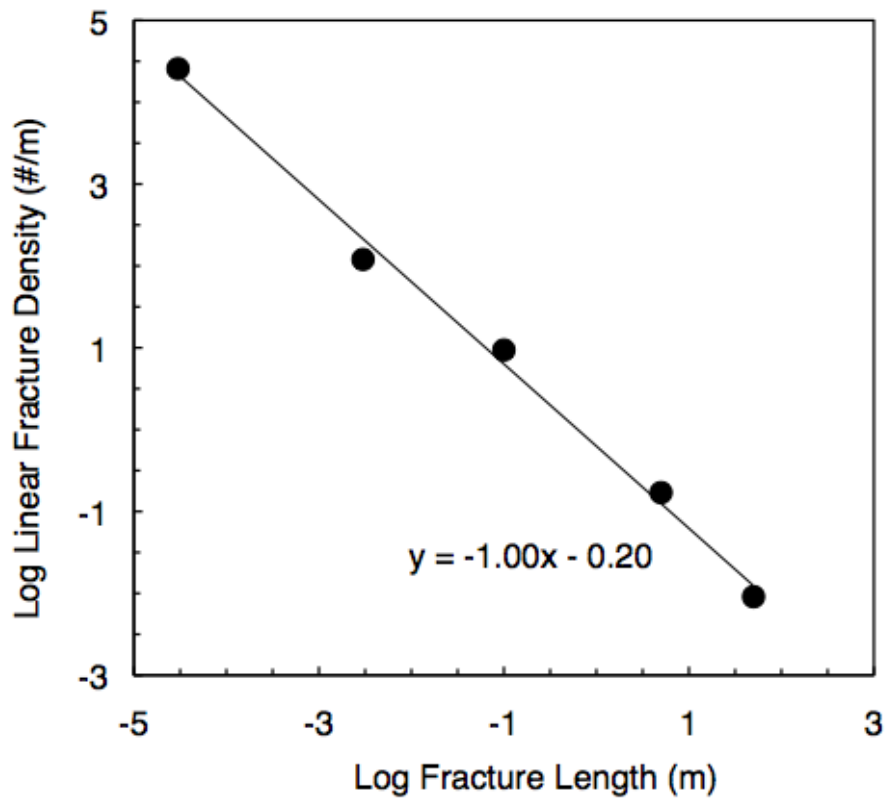
Figure 14. SAFOD Fracture density versus length at all scales. Plot of log linear fracture density versus log fracture length for SAFOD fractures across five scales of observation. Data plotted are from Table 12.
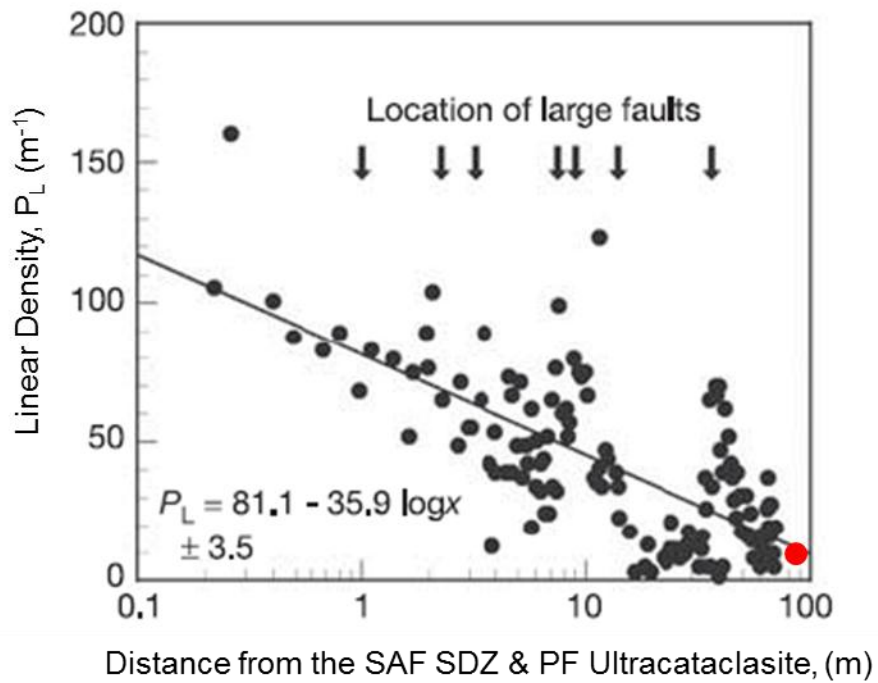
Figure 15. Transgranular fracture density of the Phase 1 arkosic sandstone core (red dot; Almeida, unpublished data, 2007) as a function of distance from the SDZ compared to the density versus log distance relationship determined for subsidiary faults in the damage zone of the Punchbowl Fault (PF). This figure is a modified version of Figure 4a in Chester et al. (2005).
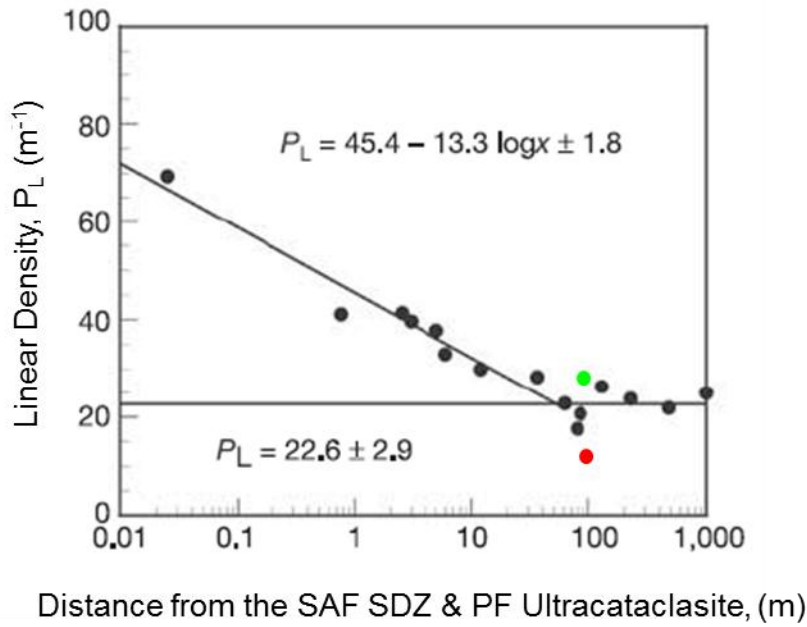
Figure 16. Intragranular fracture density of the Phase 1 Arkosic sandstone core as a function of distance from the SDZ compared to the density versus log distance relationship determined for intragranular microfractures in the damage zone of the Punchbowl Fault (PF). The red dot represents the intragranular fracture density determined using the whole thin section traverse technique (Table 6) and the green dot represents that same data corrected on the basis of the SEM-CL-Optical fracture density analysis (Tables 7-10). This figure is a modified version of Figure 4b in Chester et al. [2005].

58
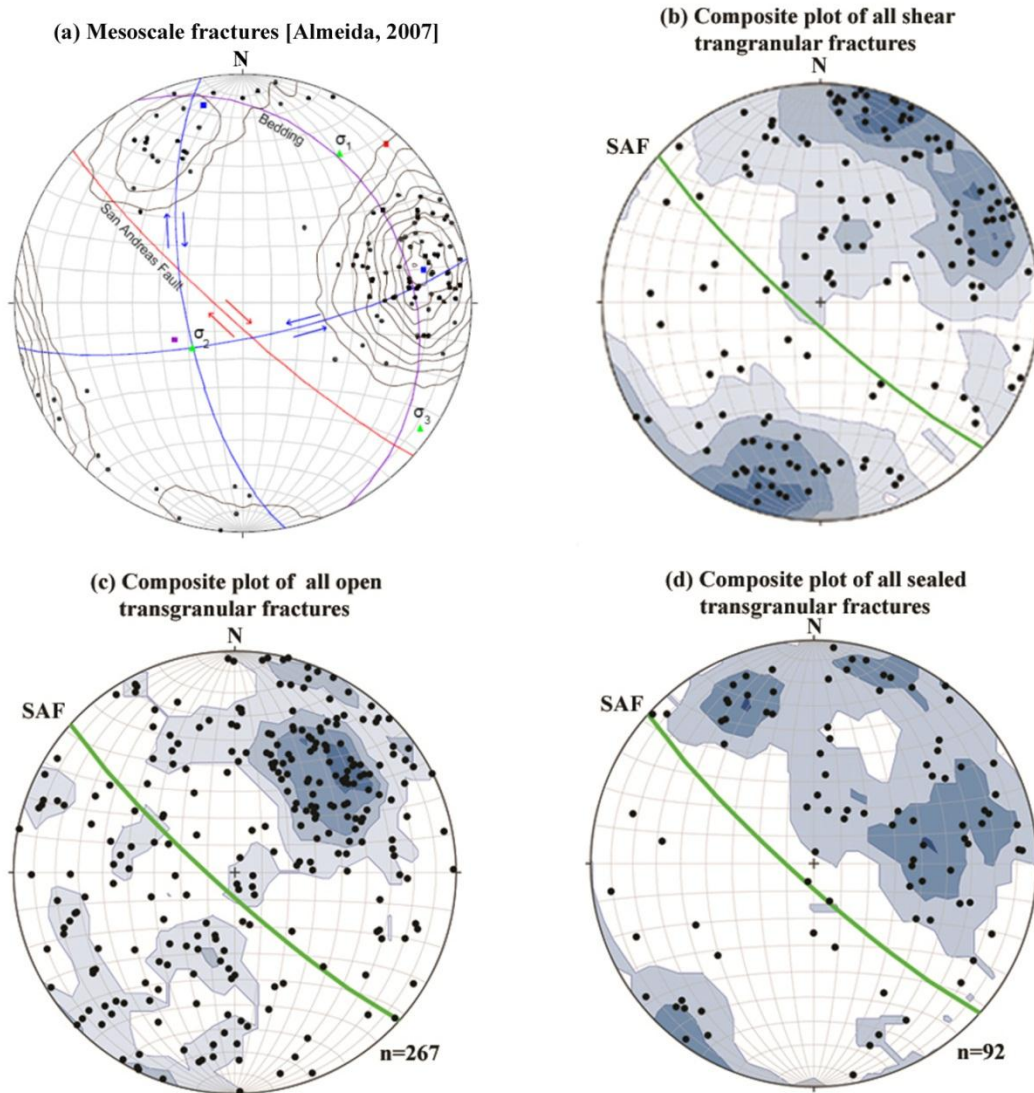
Figure 17. Orientation of transgranular shear, sealed, and open fractures from the Phase 1 arkosic sandstone samples (P1B13-1, P1B14-1, P1B16-2, P1B17-4), and of the mesoscale fractures presented in Almeida [figure 13, 2007]. Poles to fractures are plotted in a lower hemisphere equal-area projection with North (N) at top. Data are contoured with a two sigma contour interval, using the Kamb method and OSXStereonet v. 1.7 by N. Cardozo and R. Allmendinger [2011]. The plane of the SAF is shown by the red great circle. As in Almeida's figure 14 [2007], the pole to the fault at 3062 m MD is shown by the solid black circle. (a) Mesoscale fractures [modified from figure 13]. [Almeida, 2007]; (b) Composite plot of poles to all shear trangranular fractures; (c) Composite plot of poles to all open transgranular fractures; (d) Composite poles to all sealed transgranular fractures.

Table 1. Conditions of Faulting Recorded at Three Key Locations in the San Andreas System.

Fault and Rock Unit/ Faulting Conditions	San Andreas Fault Phase 1 Arkose SAFOD, CA	Punchbowl Fault Punchbowl Fm. Devils Punchbowl, CA	San Andreas Fault Juniper Hills Fm. Littlerock, CA
Effective Overburden (MPa)	30-50	22 - 45	25
Temperature (˚C)	80-135	75 - 125	< 25
Depth of Burial (km)	2-3	2 - 4	<< 1
Rock Type	Pebbly arkosic sandstone	Pebbly arkosic sandstone	Arkosic sandstone
Fault Displacement (km)	200- 300	20 - 45	19 - 21

Table 2. Structural Analyses Completed to Date at Three Faults in the San Andreas System.

Fabric Element and Scale	San Andreas Fault Phase 1 Arkose SAFOD	Punchbowl Fault Punchbowl Fm. Devils Punchbowl, CA	San Andreas Fault Juniper Hills Fm. Littlerock, CA
Mesoscale Fracture Density	R. Almeida (J. Chester, Personal communication)	Wilson et al., 2003; Chester et al.,	X
Mesoscale Fracture Fabric	Almeida, 2007	Chester & Logan, 1987	X
Transgranular Fracture Density	X	X	X
Transgranular Fracture Orientation	R. Almeida (J. Chester, Personal communication)	X	X
Intragranular Fracture Density	X	Wilson et al., 2003	Dor et al., 2009
Intragranular Fracture Orientation	R. Almeida (J. Chester, Personal communication)	Wilson et al., 2003	Dor et al., 2009

Table 3. Samples of Phase 1 Arkosic Sandstone at SAFOD Used for Fabric Analysis.

Sample Name	Thin Sections	Measured Depth (m)	Sample Type	Fracture Intensity		Fracture Orientation	CL
				WTS	INT	WTS	
P1B11-1	P1B11-1_1 to T	3057.04	AK SS	X	X	X	
	P1B11-1_B to 4		AK SS	X	X	X	
	P1B11-1_T to 4		AK SS	X	X	X	
P1B13-1	P1B13-1_3 to T	3058.82	AK SS	X	X	X	
	P1B13-1_2 to T		AK SS	X	X	X	
	P1B13-1_T to 1		AK SS	X	X	X	
P1B14-1	P1B14-1_1 to T	3059.31	AK SS	X	X	X	
	P1B14-1_4 to T		AK SS	X	X	X	
	P1B14-1_T to 1		AK SS	X	X	X	
P1B16-2	P1B16-2_3 to T	3061.64	AK SS	X	X	X	
	P1B16-2_4 to T		AK SS	X	X	X	
	P1B16-2_B to 1		AK SS	X	X	X	
P1B17-4	P1B17-4_3 to T	3062.36	AK SS	X	X	X	
	P1B17-4_2 to T		AK SS	X	X	X	
	P1B17-4_B to 1		AK SS	X	X	X	
P1B12-2	P1B12-2_3 to T	3057.65	AK SS		X		X
P1B15-1	P1B15-1_1 to T	3060.53	AK SS		X		X
P1B16-1	P1B16-1_4 to T	3061.87	AK SS		X		

AK SS = Arkosic Sandstone, X, Represents works done; WTS, Whole Thin Section; INT, Intragranular; CL, Cathodoluminescence

Table 4. Table 4. Transgranular Fracture Density Determined from Whole Thin Section Mapping (8 mm Grid).

Sample_Section	Total Count Line Length (mm)	Open Fracture Intercepts (#)	Sealed Fracture Intercepts (#)	Shear Fracture Intercepts (#)	Total Fracture Intercepts (#)	*Total Linear Fracture Density (#/mm)
P1B11-1_1-T	135.9	1	4	0	5	0.037
P1B11-1_T-4	118.0	1	2	0	3	0.025
P1B11-1_B-4	131.9	4	1	0	5	0.038
P1B11-1	**385.9**	**6**	**7**	**0**	**13**	**0.034**
P1B13-1_2-T	144.7	7	0	22	29	0.2
P1B13-1-3_T	147.3	8	6	14	28	0.19
P1B13-1-T_1	116.4	7	2	14	23	0.198
P1B13-1	**408.5**	**22**	**8**	**50**	**80**	**0.196**
P1B14-1_1-T	135.5	9	0	2	11	0.081
P1B14-1-4_T	126.0	16	18	0	34	0.27
P1B14-1-T_1	125.6	6	1	6	13	0.104
P1B14-1	**387.0**	**31**	**19**	**8**	**58**	**0.15**
P1B16-2_3-T	144.1	5	0	3	8	0.056
P1B16-2-4_T	130.7	15	3	9	27	0.207
P1B16-2-B_1	144.1	1	1	0	2	0.014
P1B16-2	**418.9**	**21**	**4**	**12**	**37**	**0.088**
P1B17-4-2_T	126.5	10	0	16	26	0.205
P1B17-4-3_T	134.6	12	0	4	16	0.119
P1B17-4-B_1	119.3	3	2	4	9	0.075
P1B17-4	**380.4**	**25**	**2**	**24**	**51**	**0.134**

*Average Total Linear Fracture Density for five samples with 3 sections is 0.120/mm.

Table 5. Transgranular Fracture Density Comparison for 8 mm- and 3 mm spaced Grids.

Thin section name	Depth (m)	Transgranular fracture density (#/mm)			# of Mesoscale Faults cutting and/or near to Samples
		Coarse (8mm) spacing	Fine (3mm) spacing	Average Density	
P1B11-1	3057.02	0.034	0.033	0.033	1
P1B13-1	3058.8	0.196	0.184	0.19	4
P1B14-1	3059.3	0.15	0.125	0.137	3
P1B16-2	3061.7	0.088	0.102	0.095	2
P1B17-4	3062.32	0.134	0.129	0.131	3

Table 6. Intragranular Fracture Density Determined from Whole Thin Section Traverse Technique.

Sample Section	Number Grains Measured	Total Count Line Length	Open Fracture Int. (#)	Healed Fracture Int. (#)	Shear Fracture Int. (#)	Total Fracture Int. (#)	*Linear Fracture Density (#/mm)
P1B11-1_1T	60	81.51	40	69	712	821	10.07
P1B11-1_B4	58	69.59	73	33	643	749	10.76
P1B11-1_T4	53	65.75	58	33	578	669	10.17
P1B11-1	**171**	**216.85**	**171**	**135**	**1933**	**2239**	**10.34**
P1B13-1_2T	60	68.89	42	31	647	720	10.45
P1B13-1_3T	57	84.10	62	83	659	804	9.56
P1B13-1_T1	59	72.36	80	48	637	765	10.57
P1B13-1	**176**	**225.35**	**184**	**162**	**1943**	**2289**	**10.19**
P1B14-1_1T	60	88.63	61	80	606	747	8.43
P1B14-1_4T	57	84.69	87	75	733	895	10.57
P1B14-1_T1	59	93.53	64	78	669	811	8.67
P1B14-1	**176**	**266.84**	**212**	**233**	**2008**	**2453**	**9.22**
P1B16-2_3T	176	181.71	193	245	1484	1922	10.58
P1B16-2_4T	60	75.79	53	39	786	878	11.59
P1B16-2_B1	59	74.95	51	55	637	743	9.91
P1B16-2	**295**	**332.45**	**297**	**339**	**2907**	**3543**	**10.69**
P1B17-4_2T	58	74.59	59	69	645	773	10.36
P1B17-4_3T	59	97.50	45	92	1026	1163	11.93
P1B17-4_B1	53	64.80	55	57	566	678	10.46
P1B17-4	**170**	**236.89**	**159**	**218**	**2237**	**2614**	**10.92**
Sections Used for SEM-CL and Optical Imaging Comparison Work							
P1B12-2_3T	64	78.29	114	53	874	1041	13.30
P1B15-1_1T	60	71.65	76	86	839	1001	13.97
P1B16-1_4T	62	92.36	117	57	885	1059	11.47

* Average Linear Fracture Density for the five samples with three sections is 10.27/mm, Int.; intercepts

Table 7. Intragranular Linear Fracture Density Comparison: SEM-CL and Flat-stage Optical Imaging for Sample P1B12-2_3-T.

Grain No.	Total Count Line Length (mm)	CL Image: Total Number of Fracture Intercepts	Optical Image: Total Number of Fracture Intercepts	CL & Optical: Total Number of Common Fracture Intercepts	True Total Number of Fracture Intercepts	True Linear Fracture Density (#/mm)
1	9.27	250	258	227	281	30.3
2	9.76	254	246	211	289	29.6
3	10.21	417	361	327	451	44.2
4	9.34	300	233	203	330	35.3
5	4.08	132	115	100	147	36.0
6	5.42	160	99	88	171	31.5
Six-Grain Average	8.01	252	219	193	278	34.7

Table 8. Correction Factors for Determining the True Intragranular Linear Fracture Density for Sample P1B12-2_3-T.

Area Measured	Linear Fracture Density from Whole Thin Section Traverse Technique (#/mm)	True Linear Fracture Density from Imaging Technique (#/mm)	Calculated Correction Factor
Grain 1	16.22	30.3	1.9
Grain 2	17.39	29.6	1.7
Grain 3	20.00	44.2	2.2
Grain 4	5.7	35.3	6.2
Grain 5	4.6	36.0	7.8
Grain 6	10.0	31.5	3.2
Six-Grain Average	12.3	34.5	2.8

*Determined using the whole-thin section traverse data (Table 6) and the true linear fracture density (Table 7).

Table 9. Intragranular Linear Fracture Density Comparison: SEM-CL and Flat-stage Optical Imaging for Sample P1B15-1_1-T.

Grain No.	Total Count Line Length (mm)	CL Image: Total Number of Fracture Intercepts	Optical Image: Total Number of Fracture Intercepts	CL & Optical: Total Number of Common Fracture Intercepts	True Total Number of Fracture Intercepts	True Linear Fracture Density (#/mm)
1	9.86	283	273	243	313	31.7
2	3.71	119	90	60	149	40.2
3	2.45	58	44	33	69	28.2
4	4.88	136	127	100	163	33.4
5	4.95	149	120	93	176	35.6
Five-Grain Average	5.17	149	131	106	174	33.7

Table 10. Correction Factors for Determining the True Intragranular Linear Fracture Density for Sample P1B15-1_1-T.

Area Measured	Linear Fracture Density from Whole Thin Section Traverse Technique (#/mm)	True Linear Fracture Density from Imaging Technique (#/mm)	Calculated Correction Factor
Grain 1	14.38	31.7	2.2
Grain 2	Not Measured	40.2	NA
Grain 3	Not Measured	28.2	NA
Grain 4	14.1	33.4	2.4
Grain 5	19.2	35.6	1.9
Six-Grain Average	15.9	33.6	2.1

*Determined using the whole-thin section traverse data (Table 6) and the true linear fracture density (Table 7).

Table 11. Linear Density of Mesoscopic Fractures in the Vicinity of the Thin Section Sample Locations.

Sample	Measured Depth (m)	Linear Density of Fractures (#/m)*
P1B11-1	3057.04	8
P1B13-1	3058.82	11
P1B14-1	3059.31	8
P1B16-2	3061.64	8
P1B17-4	3062.36	11
P1B12-2	3057.65	9
P1B15-1	3060.53	11
P1B16-1	3061.87	9

*Linear density determined from 0.6 m intervals centered on sample location using measurements of Almeida (written communication, 2006).

Table 12. Linear Fracture Density as a Function of Scale for the Arkosic Units at SAFOD.

Fabric Element (Mapping Scale)	Fracture Lengths Mapped	Mapped Area or Borehole Length	Minimum Fracture Length Counted (m)	Linear Fracture Density	Log Linear Fracture Density (#/m)
Intragranular Fractures (SEM & Optical Microscope)	30 μm to >1000 μm	10^3 mm^2	3×10^{-5}	†25.7/mm	4.41
Transgranular Fractures (Optical Microscope & Thin Section Scans)	2 mm to >30 mm	1.4×10^4 mm^2	3×10^{-3}	0.120/mm	2.08
Mesoscale Subsidiary Faults (Visual Core Surface Mapping)	>10 cm	2.0×10^6 mm^2	1×10^{-1}	9.4/m	0.97
Subsidiary Faults in Core with Gouge Layers and Juxtaposition of Contrasting Lithologies (Visual)	>5 m	11.6 m	5	0.17/m	-0.77
*Large Faults Identified by Bedding Orientation or Lithology Change in Logs (Borehole)	>100 m	1100 m	50	0.0091/m	-2.04

*Identification of faults from analysis by Draper et al. (2009) of geophysical logs from the SAFOD borehole.